Isogeometric collocation: Neumann boundary conditions and contact

L. De Lorenzis[1,*], J.A. Evans[2], T.J.R. Hughes[3], A. Reali[4]

July 1, 2014

[1]Corresponding Author.

Institut für Angewandte Mechanik, Technische Universität Braunschweig.

Bienroder Weg 87, 38106 Braunschweig, Germany.

Tel: +49 (0)531 391 94350 Fax: +49 (0)531 391 94399.

Email: l.delorenzis@tu-braunschweig.de.

[2]Aerospace Engineering Sciences, University of Colorado Boulder.

1111 Engineering Drive, Boulder, Colorado 80309-0429, USA.

[3]Institute for Computational Engineering and Sciences, University of Texas at Austin.

201 East 24th Street, Austin, Texas 78712, USA.

[4]Department of Civil Engineering and Architecture, University of Pavia.

via Ferrata 3, 27100, Pavia, Italy.

Abstract

Isogeometric collocation methods have been proposed recently and their accuracy and efficiency demonstrated for elastostatics and explicit dynamics. This paper addresses two important aspects in the development of the isogeometric collocation technology, namely, the imposition of Neumann boundary conditions and the enforcement of contact constraints, which are both treated within the same framework. It is shown that the strong imposition of Neumann boundary conditions may lead to a significant loss of accuracy in some situations, in particular when non-uniform meshes are used. Two possible remedies are proposed to restore the desired level of accuracy while keeping the computational cost virtually unchanged, i.e. a hybrid collocation-Galerkin approach and an enhanced collocation (EC) approach. A frictionless contact formulation suitable for the collocation framework is further proposed and shown to pass the contact patch test to machine precision. When combined with the EC approach, the formulation is shown to deliver accurate results and to perform robustly also for highly non-uniform meshes. For all the collocation formulations, contact pressures are greater than or equal to zero *pointwise*, in contrast with standard Lagrange finite elements.

Keywords: Isogeometric analysis; collocation methods; NURBS; boundary conditions; contact.

1 Introduction

Isogeometric analysis (IGA) was recently introduced by Hughes and coworkers (Hughes et al. 2005, Cottrell et al. 2009). Its main original purpose was to bridge the gap between computer aided design (CAD) and finite element analysis (FEA), thus simplifying the cost-intensive mesh generation process required for standard FEA and leading to a tighter integration of CAD and FEA tools. In the IGA framework, the same smooth and higher-order basis functions, e.g., non-uniform rational B-splines (NURBS) or T-splines, are used for the representation of the exact CAD geometry and for the approximation of the FEA solution fields.

In addition to the achievement of the original goal, IGA soon turned out to exhibit increased accuracy and robustness on a per-degree-of-freedom basis in comparison to standard finite element methods (FEM) (Evans et al. 2009, Großmann et al. 2012) and to possess a number of additional attractive features in several areas of computational mechanics. However, smooth higher-order basis functions immediately raised the question of their efficient implementation and, in particular, of computationally efficient quadrature rules. In Galerkin-type formulations, element-wise Gauss quadrature is considered optimal for standard FEM, but sub-optimal for IGA, since it does not exploit the inter-element continuity of its smooth basis functions. Taking advantage of the smoothness across element boundaries, more efficient quadrature rules were developed by Hughes et al. (2010) and Auricchio et al. (2012a). A natural evolution of this research was the investigation of isogeometric collocation (IGA-C) methods (Auricchio et al. 2010, 2012b), which can be interpreted as a one point quadrature rule in the IGA context.

As opposed to Galerkin formulations, collocation is based on the discretization of the strong form of the governing partial differential equations. This is only possible if basis functions of sufficient smoothness and, therefore, high order are adopted. This requirement is naturally fulfilled by the shape functions used in IGA, which feature tailorable order and inter-element continuity. Furthermore, the IGA framework allows domains of arbitrary geometric and topological complexity to be discretized, possibly in tight integration with CAD. In IGA-C, only one point evaluation per control point, or "node", is required at a collocation point. This implies the minimization of the computational effort with respect to quadrature and is a major advantage over Galerkin-type methods, especially for applications where efficiency is directly related to

the cost of quadrature. A few significant examples are explicit structural dynamics, where the computational cost is dominated by stress divergence evaluations at quadrature points for the calculation of the residual force vector, multiscale methods based on nested solution schemes such as FE^2, where a microscale boundary value problem is solved for each quadrature point of the macroscale, and stochastic approximation procedures such as the stochastic FEM, where the residual vector must be evaluated a large number of times.

One point quadrature in conjunction with low-order quadrilateral and hexahedral finite elements is already extensively (if not exclusively) used in crash dynamics and metal forming. This minimizes memory requirements and the number of constitutive evaluations and enables the efficient computation of very large problems. However, one point quadrature with standard basis functions gives rise to zero-energy hourglass modes and rank deficient system matrices (Bischoff et al. 2004). The problem is addressed by introducing artificial viscous and/or elastic stabilization mechanisms, whose parameters often require tuning by time consuming and computationally expensive sensitivity studies. Conversely, it can be shown that for quadratic and higher-order NURBS, with uniform knot vectors and a suitable choice of the collocation points, the discrete Laplace operator produced by collocation is rank sufficient in all dimensions. It follows that the elasticity operator is also rank sufficient and, in particular, there are no hourglass modes. Thus IGA-C can be viewed as a one point quadrature scheme that is rank sufficient (Auricchio et al. 2012b, Schillinger et al. 2013). Hence, IGA collocation methods eliminate the need for ad-hoc stabilization techniques. Furthermore, they show great promise for the development of higher-order accurate time integration schemes (Auricchio et al. 2012b) as well as for the development of locking-free beam, plate and shell elements (Beirão da Veiga et al. 2012, Auricchio et al. 2013).

Before a brief literature review, it is worth mentioning that collocation techniques are also quite often adopted within the framework of meshless methods, see, e.g., Oñate et al. (1996), Aluru (2000), Zhang et al. (2001), Kim and Kim (2003), Hu et al. (2007), Nguyen et al. (2008), Hu et al. (2011), Chi et al. (2013). However, the IGA-C method is *not* a meshless method; here the isoparametric concept is adopted. Meshes are employed that either have a tensor product structure or are locally refined (depending on whether NURBS or T-splines or hierarchical B-splines are adopted). In this paper, only one-patch domains with NURBS basis

functions are used in the examples. However, the extension to multi-patch NURBS domains is conceptually straightforward to obtain, at least as long as patches with matching discretizations are adopted, whereas a collocation-based framework for hierarchical B-spline discretizations has been presented by Schillinger et al. (2013).

Only a few investigations of IGA-C have been conducted thus far. Auricchio et al. (2010) developed the first one-dimensional theoretical analysis of the method, which served the dual purpose of providing the theoretical background and guiding the selection of collocation points. They presented numerical tests on simple elliptic problems in one, two and three dimensions, demonstrated the accuracy of the method, studied the behavior of the discrete eigenspectrum and discussed the performance of the scheme with respect to the choice of collocation points. Auricchio et al. (2012b) introduced a variational interpretation of the collocation scheme and set forth special considerations at points on the patch interfaces and external boundaries, giving precise descriptions of the treatment of several important cases. They also extended the framework to dynamics and described explicit predictor multi-corrector time integration algorithms. They argued that, by adopting a sufficient number of explicit multi-corrector iterations, the higher-order spatial accuracy of the corresponding implicit algorithm with consistent mass can be achieved. Finally, they presented several static and dynamic numerical examples. The method was shown to deliver satisfactory results with Dirichlet and Neumann boundary conditions, mixed boundary conditions, and on single and multi-patch configurations. In the dynamic setting, the higher-order convergence rates of the explicit multi-corrector method were demonstrated on a one-dimensional example and a two-dimensional plane strain annular configuration. Beirão da Veiga et al. (2012) adopted an IGA-C approach for the approximation of initially straight planar Timoshenko beams, and Auricchio et al. (2013) extended the investigation to curved spatial Timoshenko rods. The proposed schemes, based on standard mixed formulations, were shown theoretically and computationally to be free of shear locking for any choice of the discrete spaces for displacements, rotations, and internal forces, in contrast with most Galerkin approximation procedures. Schillinger et al. (2013) compared IGA-C with isogeometric Galerkin (IGA-G) and standard finite element methods (FEA-G) in terms of their computational efficiency. They first assessed the computational cost in floating point operations for the formation and assembly of stiffness matrices and residual vectors. The operation counts demonstrated

that IGA-C significantly reduces the computational cost compared to IGA-G and FEA-G. They also showed that in IGA-C the bandwidth of the stiffness matrix and the cost of matrix-vector products are smaller than in IGA-G and FEA-G. They then used a series of representative smooth and rough problems in 3D to numerically compare the different methods with respect to accuracy vs. the number of degrees of freedom as well as with respect to accuracy vs. the serial computing time on a single thread. The results showed that IGA-C can be orders of magnitude faster than IGA-G and FEA-G for the same level of accuracy.

From the above review it emerges that IGA-C holds significant promise to offer a more efficient alternative to existing finite element technologies. This paper focuses on two important aspects in the development of the IGA-C technology. One is the imposition of Neumann boundary conditions (bcs), and the other is the enforcement of contact constraints, which fits into the same framework when contact constraints are interpreted as deformation-dependent Neumann bcs. As will be shown subsequently, the strong imposition of Neumann bcs performed in previous investigations on IGA-C may lead to a significant loss of accuracy in some situations, in particular for problems featuring a reduced regularity of the solution and when non-uniform meshes are used. Two possible remedies to restore the desired level of accuracy while keeping the computational cost virtually unchanged are proposed in this paper. Moreover, contact formulations suitable for the collocation framework are needed to tackle problems involving interactions between multiple patches with non-conforming discretizations. A frictionless contact formulation is therefore proposed and tested herein. The formulation is developed for the fully non-linear large-deformation case, however, we confine our attention herein to linearly elastic bodies in contact. Nevertheless, we are able to exercise the formulation on demanding tests.

The paper is organized as follows. Section 2 presents a brief review of isogeometric basis functions and introduces the elastostatic problem and its treatment in the IGA-C framework. Section 3 illustrates the treatment of Neumann bcs in the conventional IGA-C setting, as well as the two alternative treatments formulated in this work. These aim at improving the accuracy of the solution in some critical cases while keeping computational cost comparable to that of the original IGA-C. Section 4 presents two examples demonstrating the possible loss of accuracy of the conventional IGA-C method and the performance of the proposed alternative procedures. Section 5 introduces the frictionless contact formulation and Section 6 illustrates four contact

examples, including two examples of contact between a deformable body and a rigid obstacle, and two examples of contact between two deformable objects, one of them consisting of the well-known contact patch test. Finally, the main conclusions are summarized in Section 7.

2 NURBS-based isogeometric collocation for elastostatics

In this section we first discuss the basic concepts regarding B-spline and NURBS basis functions, employing standard NURBS terminology. For further details and extensive references see Piegl and Tiller (1996) and Cottrell et al. (2009) among others. Subsequently, the elastostatic problem is briefly reviewed and its solution with the IGA-C formulation is presented following the variational interpretation introduced by Auricchio et al. (2012b) and Schillinger et al. (2013).

2.1 B-spline and NURBS basis functions

A B-spline basis of degree p is generated based on a sequence of real numbers called a knot vector

$$\Xi = \{\xi_1, ..., \xi_{m+p+1}\} \tag{1}$$

where $\xi_1 \leq \xi_2 \leq ... \leq \xi_{m+p+1}$, each $\xi_i \in \mathbb{R}$ is a knot, and m is the associated number of control points, also equal to the number of basis functions. A univariate B-spline basis function $N_{i,p}(\xi)$ is obtained from the so-called Cox-de Boor recursion formula. Starting from $p = 0$ where

$$N_{i,0}(\xi) = \begin{cases} 1 & \xi_i \leq \xi < \xi_{i+1} \\ 0 & \text{otherwise} \end{cases} \tag{2}$$

the basis functions for $p > 0$ are obtained from

$$N_{i,p}(\xi) = \frac{\xi - \xi_i}{\xi_{i+p} - \xi_i} N_{i,p-1}(\xi) + \frac{\xi_{i+p+1} - \xi}{\xi_{i+p+1} - \xi_{i+1}} N_{i+1,p-1}(\xi) \tag{3}$$

introducing the convention $0/0 = 0$. If a knot has multiplicity k, the smoothness of the B-spline basis is C^{p-k} at that location. In so-called open knot vectors, the first $p+1$ knots and the last $p+1$ terms are equal, so that the basis is interpolatory at the ends (Figure 1a).

Once the basis functions are available, a B-spline curve can be constructed as their linear combination

$$\mathbf{C}(\xi) = \sum_{i=1}^{m} \mathbf{P}_i N_{i,p} \tag{4}$$

where $\mathbf{P}_i \in \mathbb{R}^{d_s}$ are the so-called control points, and d_s is the dimension of the physical space (Figure 1b).

Multivariate B-splines are generated through the tensor product of univariate B-splines. If d_p denotes the dimension of the parametric space, d_p univariate knot vectors are needed:

$$\Xi^d = \left\{\xi_1^d, ..., \xi_{m_d+p_d+1}^d\right\} \tag{5}$$

where $d = 1, ..., d_p$, p_d is the polynomial degree in the parametric direction d, and m_d is the associated number of basis functions. Denoting the univariate basis functions in each parametric direction d as N_{i_d,p_d}^d, the multivariate basis functions $B_{\mathbf{i},\mathbf{p}}(\boldsymbol{\xi})$ are obtained from

$$B_{\mathbf{i},\mathbf{p}}(\xi) = \prod_{d=1}^{d_p} N_{i_d,p_d}^d\left(\xi^d\right) \tag{6}$$

where the multi-index $\mathbf{i} = \left\{i_1, ..., i_{d_p}\right\}$ denotes the position in the tensor product structure, $\mathbf{p} = \{p_1, ..., p_d\}$ indicates the polynomial degree, and $\boldsymbol{\xi} = \left\{\xi^1, ..., \xi^{d_p}\right\}$ is the vector of the parametric coordinates in each parametric direction d. B-spline surfaces and solids are obtained for $d_p = 2$ and $d_p = 3$, respectively, from a linear combination of multivariate B-spline basis functions and control points as follows

$$\mathbf{S}(\boldsymbol{\xi}) = \sum_{\mathbf{i}} \mathbf{P}_{\mathbf{i}} B_{\mathbf{i},\mathbf{p}}(\boldsymbol{\xi}) \tag{7}$$

where the summation is extended to all combinations of the multi-index $\mathbf{i}$.

NURBS basis functions are obtained from a projective transformation of their B-spline counterparts in $\mathbb{R}^{d_s+1}$. Univariate NURBS basis functions $R_{i,p}(\xi)$ are given by

$$R_{i,p}(\xi) = \frac{w_i N_{i,p}(\xi)}{\sum_{j=1}^{m} w_j N_{j,p}(\xi)} \tag{8}$$

where $N_{i,p}$ are B-spline basis functions and w_i are the corresponding weights. Finally, multivariate NURBS basis functions are obtained as

$$R_{\mathbf{i},\mathbf{p}}\left(\boldsymbol{\xi}\right) = \frac{w_{\mathbf{i}} B_{\mathbf{i},\mathbf{p}}\left(\boldsymbol{\xi}\right)}{\sum_{\mathbf{j}} w_{\mathbf{j}} B_{\mathbf{j},\mathbf{p}}\left(\boldsymbol{\xi}\right)} \tag{9}$$

and NURBS surfaces and solids result from

$$\mathbf{S}\left(\boldsymbol{\xi}\right) = \sum_{\mathbf{i}} \mathbf{P}_{\mathbf{i}} R_{\mathbf{i},\mathbf{p}}\left(\boldsymbol{\xi}\right) \tag{10}$$

2.2 Elastostatic problem

Let $\Omega \subset \mathbb{R}^{d_s}$ represent an elastic body $\mathcal{B}$ subjected to body forces $\mathbf{f}$, to prescribed displacements $\mathbf{g}$ on a portion of the boundary Γ_g, and to (possibly zero) prescribed tractions $\mathbf{p}$ on the remaining portion Γ_p. Thus $\Gamma = \Gamma_g \bigcup \Gamma_p$ is the boundary of the domain, and $\Gamma_g \bigcap \Gamma_p = \emptyset$. Suitable regularity requirements are assumed to hold for $\mathbf{f}$, $\mathbf{g}$, and $\mathbf{p}$.

The small-strain linear elasticity problem in strong form is defined by

$$\operatorname{div}\left(\mathbb{C}\nabla^S \mathbf{u}\right) + \mathbf{f} = \mathbf{0} \qquad \text{in } \Omega \tag{11}$$

complemented by the Dirichlet bcs

$$\mathbf{u} = \mathbf{g} \qquad \text{on } \Gamma_g \tag{12}$$

and by the Neumann bcs

$$\left(\mathbb{C}\nabla^S \mathbf{u}\right)\mathbf{n} = \mathbf{p} \qquad \text{on } \Gamma_p \tag{13}$$

In the above, $\mathbf{u}\left(\mathbf{x}\right)$ is the unknown displacement field ($\mathbf{x}$ being the position vector), ∇^S is the symmetric part of the gradient operator, $\mathbb{C}$ is the fourth-order elasticity tensor, div is the divergence operator, and $\mathbf{n}$ is the outward unit normal to the boundary of the domain.

2.3 Isogeometric collocation for elastostatics

As in Auricchio et al. (2012b) and Schillinger et al. (2013), the collocation method is interpreted herein in a variational sense and applied directly in the isogeometric framework. The elasticity problem in variational form, based on the principle of virtual work, reads

$$\int_\Omega \left(\mathbb{C}\nabla^S \mathbf{u}\right) : \nabla^S \mathbf{w} d\Omega = \int_\Omega \mathbf{f}\cdot\mathbf{w} d\Omega + \int_{\Gamma_p} \mathbf{p}\cdot\mathbf{w} d\Gamma \tag{14}$$

for every test function $\mathbf{w} \in \left[H^1\left(\Omega\right)\right]^{d_s}$ satisfying homogeneous Dirichlet bcs, i.e.,

$$\mathbf{w} = \mathbf{0} \qquad \text{on}\,\Gamma_g \tag{15}$$

Integrating eq. (14) by parts and rearranging terms leads to

$$\int_\Omega \left[\text{div}\left(\mathbb{C}\nabla^S \mathbf{u}\right) + \mathbf{f}\right]\cdot\mathbf{w} d\Omega - \int_{\Gamma_p} \left[\mathbb{C}\left(\nabla^S \mathbf{u}\right)\mathbf{n} - \mathbf{p}\right]\cdot\mathbf{w} d\Gamma = 0 \tag{16}$$

Note that, should the test function *not* satisfy eq. (15), we could release the Dirichlet bcs on the solution $\mathbf{u}$ and introduce a Lagrange multiplier $\boldsymbol{\lambda} \in \left[H^{-1/2}(\Gamma_g)\right]^{d_s}$ to enforce the boundary conditions weakly. The variational form of the elasticity problem would then read: find $(\mathbf{u}, \boldsymbol{\lambda}) \in \left[H^1(\Omega)\right]^{d_s} \times \left[H^{-1/2}(\Gamma_g)\right]^{d_s}$ such that

$$\begin{aligned}\int_\Omega \left(\mathbb{C}\nabla^S \mathbf{u}\right) : \nabla^S \mathbf{w} d\Omega = &\int_\Omega \mathbf{f}\cdot\mathbf{w} d\Omega + \int_{\Gamma_p} \mathbf{p}\cdot\mathbf{w} d\Gamma + \int_{\Gamma_g} \boldsymbol{\lambda}\cdot\mathbf{w} d\Gamma \\ &+ \int_{\Gamma_g} \boldsymbol{\mu}\cdot\left(\mathbf{u} - \mathbf{g}\right) d\Gamma\end{aligned} \tag{17}$$

for every test function pair $(\mathbf{w}, \boldsymbol{\mu}) \in \left[H^1(\Omega)\right]^{d_s} \times \left[H^{-1/2}(\Gamma_g)\right]^{d_s}$. Note that additional terms pertaining to the Dirichlet boundary have appeared above. If the solution $\mathbf{u}$ is sufficiently smooth (e.g., if $\mathbf{u} \in [H^2(\Omega)]^{d_s}$), then by elliptic regularity, it holds that $\mathbb{C}\left(\nabla^{\mathrm{S}}\mathbf{u}\right)\mathbf{n} \in \left[L^2(\Gamma_g)\right]^{d_s}$ and $\boldsymbol{\lambda} \equiv \mathbb{C}\left(\nabla^{\mathrm{S}}\mathbf{u}\right)\mathbf{n}$. Consequently, if $\mathbf{u}$ is sufficiently smooth, then we have

$$\int_\Omega \left(\mathbb{C}\nabla^S \mathbf{u}\right) : \nabla^S \mathbf{w} d\Omega = \int_\Omega \mathbf{f}\cdot\mathbf{w} d\Omega + \int_{\Gamma_p} \mathbf{p}\cdot\mathbf{w} d\Gamma + \int_{\Gamma_g} \mathbb{C}\left(\nabla^{\mathrm{S}}\mathbf{u}\right)\mathbf{n}\cdot\mathbf{w} d\Gamma \tag{18}$$

for every weighting function $\mathbf{w} \in [H^1(\Omega)]^{d_s}$, and integration by parts leads to eq. (16). There-

fore, if the solution is sufficiently smooth, the test function $\mathbf{w}$ does *not* need to satisfy homogeneous Dirichlet bcs in order for eq. (16) to be applicable. This property will be exploited in one of the formulations introduced later.

Using the isoparametric approach, we seek an approximation $\mathbf{u}^h$ to the unknown exact solution field $\mathbf{u}$ of the elastostatic problem in the form

$$\mathbf{u}^h = \sum_{a=1}^{n} R_a(\mathbf{x})\,\hat{\mathbf{u}}_a \tag{19}$$

where R_a are the NURBS basis functions described in Section 2 and $\hat{\mathbf{u}}_a$ are the unknown displacement control variables. Substitution into eq. (16) yields

$$\int_\Omega \left[\operatorname{div}\left(\mathbb{C}\nabla^S\mathbf{u}^h\right)+\mathbf{f}\right]\cdot\mathbf{w}d\Omega - \int_{\Gamma_p}\left[\mathbb{C}\left(\nabla^S\mathbf{u}^h\right)\mathbf{n}-\mathbf{p}\right]\cdot\mathbf{w}d\Gamma = 0 \tag{20}$$

We now need a suitable choice of the test functions. In the collocation method, the test function $\mathbf{w}$ is selected as the Dirac delta, which can be formally constructed as the limit of a sequence of smooth functions with compact support that converge to a distribution (Auricchio et al. 2010, 2012b), satisfying the so-called sifting property, i.e.,

$$\int_\Omega f_\Omega(\mathbf{x})\,\delta(\mathbf{x}-\mathbf{x}_i)\,d\Omega = f_\Omega(\mathbf{x}_i) \tag{21}$$

$$\int_\Gamma f_\Gamma(\mathbf{x})\,\delta(\mathbf{x}-\mathbf{x}_i)\,d\Gamma = f_\Gamma(\mathbf{x}_i) \tag{22}$$

for every function f_Ω continuous about the point $\mathbf{x}_i \in \Omega$ and for every function f_Γ continuous about the point $\mathbf{x}_i \in \Gamma$. In the following, the Dirac delta will be indicated as a Dirac delta "function" following conventional terminology.

Let us assume that $d_s = 2$, m_1 and m_2 are the numbers of control points in the two parametric directions and $n = m_1 m_2$ is the total number of control points. Thus $2n$ scalar equations are needed to determine the unknown control point displacements. In the collocation scheme, we choose n collocation points τ_{kl}, $k = \{1, ..., m_1\}$, $l = \{1, ..., m_2\}$ located at the (tensor product) Greville or Demko abscissae (Auricchio et al. 2010 and references therein) of the knot vectors. The collocation points for $k = 1, m_1$ and $l = 1, m_2$ are located at the boundary Γ. Separate sets

of equations are needed for the patch interior and for the boundaries.

In the patch interior Ω, we write $2\left(m_1-2\right)\left(m_2-2\right)$ scalar equations by choosing as test functions the Dirac delta functions centered at the interior collocation points τ_{kl}, $k=\{2,...,m_1-1\}$, $l=\{2,...,m_2-1\}$. The resulting equations read

$$\left[\text{div}\left(\mathbb{C}\nabla^S\mathbf{u}^h\right)+\mathbf{f}\right]\left(\tau_{kl}\right)=\mathbf{0}\qquad\tau_{kl}\subset\Omega \tag{23}$$

i.e., they are the collocated strong form of the equations at τ_{kl}.

No equations are needed at the Dirichlet boundary, as we impose *a priori* that $u_i^h\left(\tau_{kl}\right)=g_i\left(\tau_{kl}\right)$ on Γ_g.

3 Collocation, hybrid collocation - Galerkin and enhanced collocation treatments for the enforcement of Neumann bcs

Three possible methods to enforce Neumann bcs within the IGA-C framework are described. As illustrated in the later examples, the standard collocation treatment utilized in prior literature on isogeometric collocation may deliver results of unsatisfactory accuracy in certain situations, for which reason the two alternative formulations are proposed in this paper.

3.1 Collocation treatment

In the standard collocation method, each $\tau_{kl}\subset\Gamma_p$ is associated with a collocation equation that sets the value of the boundary traction. This corresponds to choosing as test functions the Dirac delta functions centered at the collocation points located at the Neumann boundary. Here a distinction is needed between the collocation points located at the edges ($k=1,m_1$ and $l=2,...,m_2-1$, or $l=1,m_2$ and $k=2,...,m_1-1$), and those located at the corners of the domain ($k=1,m_1$ and $l=1,m_2$). For collocation points located on edges within the Neumann boundary, the equations are

$$\left[\mathbb{C}\left(\nabla^S \mathbf{u}^h\right)\mathbf{n} - \mathbf{p}\right](\tau_{kl}) = \mathbf{0} \qquad \tau_{kl} \subset \text{edge} \subset \Gamma_p \tag{24}$$

i.e., they are the collocated strong form of the Neumann bcs at τ_{kl}. For collocation points located at corners where two Neumann boundaries meet, Auricchio et al. (2012b) showed that the appropriate equations are

$$\left[\mathbb{C}\left(\nabla^S \mathbf{u}^h\right)\mathbf{n}' - \mathbf{p}'\right](\tau_{kl}) + \left[\mathbb{C}\left(\nabla^S \mathbf{u}^h\right)\mathbf{n}'' - \mathbf{p}''\right](\tau_{kl}) = \mathbf{0} \qquad \tau_{kl} \equiv \text{corner} \subset \Gamma_p \tag{25}$$

where $\mathbf{n}'$ and $\mathbf{n}''$ are the outward unit normals of the edges meeting at the corner, and $\mathbf{p}'$ and $\mathbf{p}''$ are the respective imposed tractions.

The approach in which collocation equations are written at the patch interior (eq. (23)) and at the Neumann boundary (eq. (25)) is denoted in the following as the "basic collocation" (BC) approach. It coincides with the approach proposed in the first investigations on IGA-C methods, see Auricchio et al. (2012b). In what follows, it will be shown that the BC approach may lead to an inaccurate imposition of the Neumann bcs and therefore alternative methods are needed.

3.2 Hybrid collocation - Galerkin treatment

In this approach, the equations at the Neumann boundary are written by choosing as test functions some of the shape functions used for the discretization of the unknown displacements. Let us consider the collocation points located on the Neumann boundary at an edge. E.g., at an edge with $k = \bar{k} = 1, m_1$ and $l = 2, ..., m_2 - 1$ we can write $2\,(m_2 - 2)$ equations by choosing as test functions the shape functions R_b with $b = m_1\,(l-1) + \bar{k}$, as follows

$$\int_\Omega \left[\text{div}\left(\mathbb{C}\nabla^S \mathbf{u}^h\right) + \mathbf{f}\right] R_b d\Omega - \int_{\Gamma_{p\bar{k}}} \left[\mathbb{C}\left(\nabla^S \mathbf{u}^h\right)\mathbf{n}_{\bar{k}} - \mathbf{p}_{\bar{k}}\right] R_b d\Gamma = \mathbf{0} \tag{26}$$

where $\Gamma_{p\bar{k}}$ denotes the considered edge within the Neumann boundary, and $\mathbf{n}_{\bar{k}}$ and $\mathbf{p}_{\bar{k}}$ are the respective outward unit normal and applied traction. In the same way, at edges with $l = \bar{l} = 1, m_2$ and $k = 2, ..., m_1 - 1$, we can write $2\,(m_1 - 2)$ equations by choosing as test functions the shape functions R_c, with $c = m_1\left(\bar{l} - 1\right) + k$, i.e.

$$\int_{\Omega} \left[\text{div}\left(\mathbb{C}\nabla^S \mathbf{u}^h\right) + \mathbf{f}\right] R_c d\Omega - \int_{\Gamma_{p\bar{l}}} \left[\mathbb{C}\left(\nabla^S \mathbf{u}^h\right) \mathbf{n}_{\bar{l}} - \mathbf{p}_{\bar{l}}\right] R_c d\Gamma = \mathbf{0} \tag{27}$$

where the considered edge is indicated as $\Gamma_{p\bar{l}}$, and $\mathbf{n}_{\bar{l}}$ and $\mathbf{p}_{\bar{l}}$ are the respective outward unit normal and applied traction. Note that the shape functions R_b and R_c are those corresponding to the control points located on the Neumann edges of the patch domain.

The integrals in eqs. (26) and (27) can be evaluated with Gauss-Legendre quadrature. Note that, while all NURBS shape functions have support over $(p+1)(q+1)$ knot spans, those pertaining to the control points located at the edges have a reduced support in the parametric direction perpendicular to the edges due to the use of open knot vectors. In particular, shape functions R_b have support over $(1)(q+1)$ knot spans, i.e., over knot intervals $[\xi_{p+1}, \xi_{p+2}] \times [\eta_l, \eta_{l+q+1}]$ for $\bar{k} = 1$ and over knot intervals $[\xi_{m_1}, \xi_{m_1+1}] \times [\eta_l, \eta_{l+q+1}]$ for $\bar{k} = m_1$. Shape functions R_c have support over $(p+1)(1)$ knot spans, i.e., over knot intervals $[\xi_k, \xi_{k+p+1}] \times [\eta_{q+1}, \eta_{q+2}]$ for $\bar{l} = 1$ and over knot intervals $[\xi_k, \xi_{k+p+1}] \times [\eta_{m_2}, \eta_{m_2+1}]$ for $\bar{l} = m_2$.

The approach in which collocation equations are written at the patch interior (eq. (23)) whereas Galerkin-like equations are written at the Neumann boundary (eqs. (26) or (27)) is denoted in the following as "hybrid collocation" (HC), to emphasize that it is a hybrid of collocation and Galerkin test functions. Due to the need for the evaluation of the integrals in eqs. (26) or (27), the HC approach is somewhat more expensive than the BC approach. However, it retains a significant cost advantage relative to the conventional Galerkin method, as the equations at the interior points are still written in the collocated form (23). Moreover, this approach will be later shown to achieve in certain situations better accuracy than the BC method for non-uniform meshes.

3.3 Enhanced collocation treatment

As mentioned earlier and shown later in the examples, the use of the BC collocation approach leads in some cases to unsatisfactory accuracy of the results in presence of Neumann bcs. The HC treatment presented in the previous section yields improved results but requires integration over both the area and edge domains (eqs. (26) or (27)). The enhanced collocation approach is meant to mimic the results of the HC approach while maintaining the same computational cost

as pure collocation. As in the HC case, the Neumann bcs are written considering a combination of area and edge terms, as follows

$$\left[\text{div}\left(\mathbb{C}\nabla^S\mathbf{u}^h\right)+\mathbf{f}\right](\tau_{kl})-\frac{C^*}{h}\left[\mathbb{C}\left(\nabla^S\mathbf{u}^h\right)\mathbf{n}-\mathbf{p}\right](\tau_{kl})=\mathbf{0}\qquad \tau_{kl}\subset\text{edge}\subset\Gamma_p \tag{28}$$

where h is the mesh size in the direction perpendicular to the edge. This size is here computed as the distance between the first two collocation points encountered starting from the edge and traveling in the parametric direction perpendicular to the edge. In order for this approach to be applicable, a suitable value for the constant C^* in eq. (28) needs to be determined. The constant C^* is here calibrated by minimizing the discrepancy of the results with respect to those obtained with the classical Galerkin formulation. This will be illustrated in detail in Section 4.

The approach in which collocation equations are written at the patch interior (eq. (23)) whereas enhanced collocation equations are written at the Neumann boundary (eq. (28)) is denoted in the following as "enhanced collocation" (EC).

4 Examples of the enforcement of Neumann bcs

In this section, some examples are presented to illustrate the performance of the previously described methods for small-strain linear elasticity problems in plane strain. For simplicity we will always consider single-patch situations. However, the extension to multiple patches can be easily dealt with as shown by Auricchio et al. (2012b), see also Schillinger et al. (2013).

4.1 Example N1: the compression test

4.1.1 Description and general results

The first example is a square block of side $L = 1$. The lower edge has restrained displacements in both directions, whereas the upper edge has restrained displacement in the horizontal direction and a constant downward imposed displacement in the vertical direction, $\bar{v}$. The vertical sides are both subjected to homogeneous Neumann bcs in both directions (Figure 2). The material has Lamè constants $\mu = 0.5$ and $\lambda = 0.8$. Despite the assumption of small-strain elasticity, the quite large vertical downward displacement $\bar{v} = -0.25$ is applied to help visualize the effects of

the different numerical treatments on results.

A crucial parameter influencing the collocation performance is the geometry of the mesh. As shown hereafter, the strong enforcement of Neumann bcs leads to inaccurate results when the distance between consecutive collocation points perpendicular to the boundary is sufficiently larger than parallel to the boundary. For simplicity, in the following this parameter is controlled indirectly through the ratio between the number of control points in the directions parallel and perpendicular to the Neumann boundary, which we will refer to as the "mesh aspect ratio" for the sake of simple terminology. E.g., a mesh with 10x20 control points for the example in Figure 2 is said to have an aspect ratio of 2.

Figure 3 shows the contour plot of the vertical displacement component on the deformed shape, as obtained from the BC, HC and EC formulations. For aspect ratios larger than 1, BC results are characterized by significant oscillations of the solution field close to the Neumann boundaries (Figure 3b,c). These oscillations result from the strong enforcement of the Neumann bcs and tend to increase with increasing mesh aspect ratio. Both the HC and the EC treatments solve the issue recovering good-quality displacement contour plots and deformed shapes.

Note that this behavior emanates from the large gradients of deformations and stresses in proximity of the corners. No oscillations are registered if the same example is computed with Poisson's ratio $\nu = 0$ or with unrestrained horizontal displacements on the upper and lower edges of the block, regardless of the mesh aspect ratio. Interestingly, examples with such localized strain and stress gradients at the corners due to the particular choice of the bcs also feature a reduced theoretical regularity of the solution; see Grisvard (2011) and the convergence plots in the next section. Similar oscillations had never been observed in previous investigations on IGA-C, as problems attaining a solution with full regularity and uniform meshes had always been adopted.

4.1.2 Convergence behavior

We shall perform an evaluation of the displacement errors for the BC, HC and EC methods, as well as for the Galerkin method. As no closed-form solution is available for the present example, the reference solution is computed for a mesh with degree 5 in both parametric directions, uniform knot vectors and 200x200 control points solved with the Galerkin method. The normalized

displacement error in the L_2-norm is evaluated as follows

$$e_{L^2}^{Ref} = \frac{\left\|\mathbf{u}^h - \mathbf{u}^{ref}\right\|_{L^2}}{\left\|\mathbf{u}^{ref}\right\|_{L^2}} \tag{29}$$

where $\mathbf{u}^{ref}$ is the reference displacement solution. Figure 4 shows the convergence plots for discretizations of different order with aspect ratios of 1 and 5, in order to quantify the role of the aspect ratio on the convergence behavior.

A few noteworthy observations emerge:

- all convergence plots feature a slope close to 1.5 for second-order discretizations, and slightly larger (up to a maximum of about 2 in the fifth-order case) for higher orders. The suboptimal convergence rates are due to the reduced regularity caused by the particular bcs; see e.g. Grisvard (2011). The theoretically expected slope of the convergence plot is given by the solution α of the following non-linear equation (Grisvard 1986)

$$\sin^2\left(\frac{\pi}{2}\alpha\right) = \frac{(\lambda+2\mu)^2 - (\lambda+\mu)^2\,\alpha^2}{(\lambda+\mu)\,(\lambda+3\mu)} \tag{30}$$

  which is equal to about 1.7 for this case;

- when the aspect ratio is equal to 1, there are no significant differences in the convergence behavior of the BC, HC and EC approaches, except for the highest analyzed orders where BC delivers a slightly lower accuracy than the other methods;

- when the aspect ratio is equal to 5, BC results are in all cases significantly less accurate than those of the other methods;

- for orders 2 and 3, the Galerkin approach outperforms the others. For orders 4 and 5 and regardless of the mesh aspect ratio, HC and EC deliver the same accuracy as the Galerkin method, at a significantly lower computational cost.

4.1.3 Comparison of methods

Since convergence plots show that the error of the Galerkin method is always the smallest, in this section the quality of all methods is evaluated through the comparison with results obtained from the Galerkin method on the same discretization. In particular, the displacement error of each method *relative to the Galerkin solution* is computed as

$$e_{L^2}^{Gal} = \frac{\left\|\mathbf{u}^h - \mathbf{u}_G^h\right\|_{L^2}}{\left\|\mathbf{u}_G^h\right\|_{L^2}} \tag{31}$$

where $\mathbf{u}_G^h$ is the Galerkin solution for any given mesh. The above quantity is evaluated as a function of the mesh aspect ratio by fixing the number of control points in one direction and increasing their number in the other direction. The change in quality of the solution as a result of the change in the number of degrees of freedom does not affect the evaluation as the comparison with Galerkin results is always made for the same mesh. Results are shown in Figure 5.

As is visibile in Figure 5a,b, BC leads to a displacement error relative to Galerkin which increases significantly as the mesh aspect ratio is increased for all interpolation orders. If collocation is performed at the Demko abscissae (Figure 5b) the error monotonically increases with the interpolation order for a given mesh aspect ratio. If Greville abscissae are used (Figure 5a) a similar trend is observed with the exception of the second-order case, which shows a different behavior.

Figures 5c-f indicate that both the HC and the EC formulations (whereby the choice of $C^* = 4$ will be justified later) reduce the error relative to Galerkin by more than one order of magnitude, to a level which varies weakly with the mesh aspect ratio and with the interpolation order. The errors resulting from the HC and EC formulations are very similar, whereby EC is computationally as (in)expensive as BC whereas HC requires computation of the boundary integrals. On the other hand, calibration of the unknown constant C^* is needed for EC. We expand upon this issue in the next sub-section.

4.1.4 Choice of C^* in the EC treatment

As mentioned earlier, the EC treatment requires the constant C^* to be appropriately selected. For this example, the selection of C^* based on minimization of the displacement error as given by Eq. (31) is illustrated in Figure 6. For the sake of conciseness only results obtained from collocation at the Greville abscissae are reported, however very similar results were obtained from the use of the Demko abscissae. It is clear that $e_{L^2}^{Gal}$ exhibits a definite minimum, so that the "optimal" value of C^* is readily estimated. For a given degree of the interpolation, the optimal C^* depends weakly on the mesh aspect ratio and seems to attain a constant value as the

aspect ratio becomes sufficiently large (Figure 7). If this constant value is plotted as a function of the interpolation degree (Figure 8), the obtained trend is increasing when Greville abscissae are used, and approximately constant for Demko abscissae. To verify whether the optimal C^* correctly scales with h as assumed in Eq. (28), analyses in Figures 6-7 (all based on a minimum number of control points fixed to 10 and hence, for aspect ratios larger than unity, on a fixed value of h) have been repeated for a minimum number of control points equal to 20. As shown in Figure 8, results show a satisfactory agreement between the two curves for both Greville and Demko abscissae.

The final results indicate that a value of C^* between 3 and 4 can be considered appropriate for all interpolation degrees using both Greville and Demko abscissae. The errors shown in Figure 5 have been computed for $C^* = 4$ thus verifying that low errors are obtained in all cases. Note that the optimal value of C^* is expected to be operator-dependent but not problem-dependent, so that the calibration performed herein is expected to hold for all small-strain elasticity problems. This is verified in the next example.

4.2 Example N2: the quarter of annulus

4.2.1 Description and general results

The second example is a quarter of an annulus of inner radius $R_i = 1$ and outer radius $R_o = 4$. The left vertical side has restrained displacements in both directions, whereas the lower horizontal side has restrained displacement in the vertical direction and a constant imposed displacement, $\bar{u}$, in the horizontal direction. The curved sides are both subjected to homogeneous Neumann bcs in both directions (Figure 9). The material has Lamé constants $\mu = 0.5$ and $\lambda = 0.8$. A horizontal displacement $\bar{u} = 1.00$ is imposed.

Figure 10 shows the contour plot of the vertical displacement component on the deformed shape, as obtained from the BC, HC and EC formulations. As in the previous example, BC results for aspect ratios larger than one exhibit significant spurious oscillations of the solution field close to the Neumann boundaries (Figure 10b,c). These oscillations disappear when either the HC or the EC formulation is adopted. Figure 11 is analogous to Figure 10 but here meshes have twice the number of control points in each direction. It is evident that mesh refinement

reduces the size of the spurious oscillations, which become more localized in the vicinity of the corners. Once again these oscillations are only visibile in the BC results and disappear when HC or EC are used.

4.2.2 Convergence behavior

Once again, we evaluate the displacement error of the BC, HC, EC and Galerkin methods, and employ an "overkill" solution computed with the Galerkin method on a mesh with degree 5 in both parametric directions, uniform knot vectors and 200x200 control points. The normalized displacement error in the L_2-norm is evaluated from eq. (29). Figure 12 shows the convergence plots of the displacements for discretizations of different orders for aspect ratios of 1 and 5. The main observations are summarized as follows:

- as in the previous example, the reduced regularity of the solution, due to the particular form of the bcs, leads to convergence rates between 1.5 and 2, which is consistent with the anticipated theoretical rate of about 1.7 (once again from eq. (30));
- regardless of the aspect ratio, the Galerkin method is always the most accurate. For orders 2 and 3 BC, EC and HC deliver approximately the same accuracy;
- when the aspect ratio is equal to 1 and for orders 4 and 5, the HC method is the least accurate, the BC method is intermediate and the EC method is more accurate and asymptotically approaches the same accuracy of the Galerkin method;
- when the aspect ratio is equal to 5 and for orders 4 and 5, BC is the least accurate, whereas EC and HC deliver approximately the same accuracy which asymptotically approaches the accuracy of the Galerkin method;
- to sum up, for orders 2 and 3 the Galerkin approach outperforms the others. For orders 4 and 5 and regardless of the mesh aspect ratio, EC delivers the same accuracy as the Galerkin method, at a significantly lower computational cost. Thus EC appears as the best choice among collocation methods, and its accuracy comes close to that of the Galerkin method as the order increases.

4.2.3 Comparison of methods

As in the previous example, BC leads to a displacement error *relative to the Galerkin solution* which increases for larger values of the mesh aspect ratio (Figure 13). For both the Demko and Greville abscissae, for a given aspect ratio, the error monotonically increases with p for $p \geq 3$. However, $p = 2$ does not fit this trend for either the Demko or Greville abscissae.

Figures 13c-f indicate that both the HC and the EC formulations (once again the choice of $C^* = 4$ will be justified later) reduce the error relative to Galerkin with respect to the BC method. As in the first example, HC and EC deliver similar results for non-uniform meshes. They both lead to a reduced error which varies weakly with the mesh aspect ratio and with the interpolation order.

4.2.4 Choice of C^* in the EC treatment

As mentioned earlier, the optimal value of the constant C^* is expected to be operator-dependent and not problem-dependent. Therefore we expect the optimal C^* for this second example to also lie in the range between 3 and 4 as indicated by the first example. Figure 14 illustrates $e_{L^2}^{Gal}$ as a function of C^* for different mesh aspect ratios and different interpolation degrees. The minimum is here less definite than in the previous example, especially for interpolations of higher degree. This is advantageous as it indicates a limited sensitivity of the results to the actual choice of C^*. The optimal C^* is reported in Figure 15 as a function of the mesh aspect ratio. For a given degree of interpolation, the optimal C^* weakly increases with the aspect ratio and does not reach a plateau as in the first example. However, the corresponding variations of the error are of negligible magnitude. In Figure 16, the optimal C^* corresponding to a mesh aspect ratio of 5 is plotted as a function of the interpolation degree. The obtained trend is more irregular than in the first example, especially for low order interpolations as these feature a very flat shape of the error curve as a function of C^*. Despite the seemingly large range of variation of the optimal C^*, a constant value of 4 is verified in Figure 13 to yield a very limited variation of the error with the mesh aspect ratio and with the interpolation order.

Scaling of the optimal C^* with h has also been verified in this example by doubling the minimum number of control points in the mesh. Figure 16 shows the two sets of results. The

seemingly large difference for low interpolation orders is once again connected to the flat shape of the curve of $e_{L^2}^{Gal}$ vs. C^*, and has no practical consequences as the change in error corresponding to choices of C^* deviating from the optimal value is negligible.

The final results indicate that, for second- and third-degree interpolations, any value of C^* above 2 can be considered adequate, whereas for higher-order interpolations a value between 1.5 and 4 would be advisable. This also confirms that the value of $C^* = 4$ identified from the first example is still applicable to a different test case based on the same elasticity operator.

5 Contact formulation

As mentioned earlier, the second objective of this contribution is to extend the treatment of Neumann bcs to the description of contact between multiple patches with non-matching discretizations within the IGA-C framework. This section first introduces the frictionless contact problem between deformable bodies, in strong as well as in variational form. Subsequently, we illustrate the treatment of contact constraints within IGA-C based upon the three alternative formulations presented earlier for the enforcement of Neumann bcs.

5.1 Elastostatic problem with frictionless contact

Let $\Omega^{(i)} \subset \mathbb{R}^{d_s}$, $i = 1, 2$, represent two elastic bodies $\mathcal{B}^{(i)}$, each subjected to body forces $\mathbf{f}^{(i)}$, to prescribed displacements $\mathbf{g}^{(i)}$ on a portion of the boundary $\Gamma_g^{(i)}$, to (possibly zero) prescribed tractions $\mathbf{p}^{(i)}$ on a portion of the boundary $\Gamma_p^{(i)}$, and to contact constraints on the remaining portion $\Gamma_c^{(i)}$. Thus $\Gamma^{(i)} = \Gamma_g^{(i)} \bigcup \Gamma_p^{(i)} \bigcup \Gamma_c^{(i)}$ is the boundary of the domain $\Omega^{(i)}$, and $\Gamma_g^{(i)} \bigcap \Gamma_p^{(i)} = \Gamma_g^{(i)} \bigcap \Gamma_c^{(i)} = \Gamma_p^{(i)} \bigcap \Gamma_c^{(i)} = \emptyset$. Suitable regularity requirements are assumed for $\mathbf{f}^{(i)}$, $\mathbf{g}^{(i)}$, and $\mathbf{p}^{(i)}$. Note that $\Gamma_c^{(1)} \neq \Gamma_c^{(2)}$ in general, whereas the respective mappings in the current configuration during contact coincide: $\gamma_c^{(1)} = \gamma_c^{(2)}$. The deformations are assumed small, however, the displacements are used to update the geometry to discern contact.

The small-strain linear elasticity problem in strong form for the two bodies consists of the balance equations

$$\operatorname{div}\left(\mathbb{C}^{(i)} \nabla^S \mathbf{u}^{(i)}\right) + \mathbf{f}^{(i)} = \mathbf{0} \quad \text{in}\, \Omega^{(i)} \tag{32}$$

complemented by the Dirichlet bcs

$$\mathbf{u}^{(i)} = \mathbf{g}^{(i)} \qquad \text{on}\, \Gamma_g^{(i)}, \tag{33}$$

by the Neumann bcs

$$\left(\mathbb{C}^{(\mathrm{i})} \nabla^S \mathbf{u}^{(i)}\right) \mathbf{n}^{(i)} = \mathbf{p}^{(i)} \qquad \text{on}\, \Gamma_p^{(i)} \tag{34}$$

and by the unilateral frictionless contact conditions

$$g_N \leq 0 \qquad t_N \geq 0 \qquad g_N t_N = 0 \tag{35}$$

In the above, all quantities with superscript (i) refer to body $\mathcal{B}^{(i)}$. The normal gap and normal contact traction are defined as (Laursen 2002, Wriggers 2006)

$$g_N = \left(\mathbf{x}^{(s)} - \bar{\mathbf{x}}^{(m)}\right) \cdot \bar{\mathbf{n}}^{(m)} \qquad t_N = \mathbf{t} \cdot \bar{\mathbf{n}}^{(m)} \tag{36}$$

where $\mathbf{x}^{(i)} = \mathbf{X}^{(i)} + \mathbf{u}^{(i)}$ are the current coordinates of a point of body $\mathcal{B}^{(i)}$ ($\mathbf{X}^{(i)}$ being the reference coordinates) and $\mathbf{t}$ is the contact traction vector, whereas the superscripts (s) and (m) refer to the slave and master surfaces, respectively, and the symbol $\bar{(\cdot)}$ denotes the closest point projection from the slave onto the master surface. Thus $\bar{\mathbf{n}}^{(m)}$ is the normal to the master surface at the (normal) projection point $\bar{\mathbf{x}}^{(m)}$ of a point $\mathbf{x}^{(s)}$ on the slave surface. Note that the choice to conduct the projection in the orthogonal direction to the master surface (and not to the slave surface) is well established as it yields advantages in the consistent linearization of the contact terms (Laursen 2002, Wriggers 2006). In the formulation adopted herein, each surface is taken alternatively as slave and master according to the so-called two-half-pass algorithm (Sauer and De Lorenzis, 2013). This differs from the classical contact treatments where one surface is chosen as master and the other one as slave. More details are reported in Section 5.5.

5.2 Variational formulation

The weak form of the balance equation (11) is

$$G\left(\mathbf{u},\mathbf{w}\right)=\sum_{i=1}^{2}G_i\left(\mathbf{u}^{(i)},\mathbf{w}^{(i)}\right)+G_c=0 \tag{37}$$

where

$$G_i=\int_{\Omega^{(i)}}\left(\mathbb{C}^{(\mathrm{i})}\nabla^S\mathbf{u}^{(i)}\right):\nabla^S\mathbf{w}^{(i)}d\Omega-\int_{\Omega^{(i)}}\mathbf{f}^{(i)}\cdot\mathbf{w}^{(i)}d\Omega-\int_{\Gamma_p^{(i)}}\mathbf{p}^{(i)}\cdot\mathbf{w}^{(i)}d\Gamma \tag{38}$$

and

$$G_c=-\sum_{i=1}^{2}\int_{\Gamma_c^{(i)}}\mathbf{t}^{(i)}\cdot\mathbf{w}^{(i)}d\Gamma \tag{39}$$

where $\mathbf{w}^{(i)}$ are the test functions which are assumed to be of sufficient regularity and to satisfy the homogeneous Dirichlet bcs

$$\mathbf{w}^{(i)}=\mathbf{0}\qquad\qquad\text{on}\,\Gamma_g^{(i)} \tag{40}$$

Integrating by parts and rearranging terms leads to

$$\sum_{i=1}^{2}\left[\int_{\Omega^{(i)}}\left[\mathrm{div}\left(\mathbb{C}^{(\mathrm{i})}\nabla^S\mathbf{u}^{(i)}\right)+\mathbf{f}^{(i)}\right]\cdot\mathbf{w}^{(i)}d\Omega-\int_{\Gamma_p^{(i)}}\left[\mathbb{C}^{(\mathrm{i})}\left(\nabla^S\mathbf{u}^{(i)}\right)\mathbf{n}^{(i)}-\mathbf{p}^{(i)}\right]\cdot\mathbf{w}^{(i)}d\Omega\right.$$
$$\left.-\int_{\Gamma_c^{(i)}}\left[\mathbb{C}^{(\mathrm{i})}\left(\nabla^S\mathbf{u}^{(i)}\right)\mathbf{n}^{(i)}-\mathbf{t}^{(i)}\right]\cdot\mathbf{w}^{(i)}d\Gamma\right]=0 \tag{41}$$

Once again, should $\mathbf{w}^{(i)}$ not satisfy the homogeneous Dirichlet bcs, an additional term stemming from the Dirichlet bounday would appear in eq. (38). However, this term would cancel out during integration by parts, leading again to eq. (41). This justifies the choice of test functions not vanishing on the Dirichlet boundary in the HC approach. The discretized version of eq. (41) is obtained through the use of eq. (19).

5.3 Pure collocation, hybrid collocation-Galerkin and enhanced collocation enforcement of contact constraints

Herein, contact constraints are treated as deformation-dependent Neumann bcs and thus enforced with the three methods presented in Section 3. The corresponding equations are obtained by simply substituting the known pressure $\mathbf{p}$ at the Neumann boundary with the contact traction, which is *a priori* unknown and depends on the deformation of the two bodies. The computation of the contact traction depends on the solution method chosen for the enforcement of the contact constraints. The simplest option, adopted herein, is the penalty method, which yields

$$\mathbf{t} = -\varepsilon_N g_N \bar{\mathbf{n}}^{(m)} \tag{42}$$

where $\varepsilon_N > 0$ is the so-called penalty parameter. With this method the non-penetration constraint is enforced exactly in the limit as ε_N approaches infinity. For a correct scaling, the penalty parameter should be in turn set as $\varepsilon_N = \bar{\varepsilon}_N / h$, with $\bar{\varepsilon}_N$ as a constant and h as a characteristic mesh size.

As the active contact boundary is *a priori* unknown, an active set strategy is needed in order to determine the active collocation points. According to the definition of the normal gap in eq. (36), $g_N \leq 0$ needs to be determined at all points at which penetration of the bodies takes place (Laursen 2002, Wriggers 2006).

In the BC method, each $\tau_{kl} \subset \Gamma_c$ is associated with a collocation equation that sets the value of the contact traction. This once again corresponds to choosing as test functions the Dirac delta functions centered at the collocation points located within the contact boundary. The resulting equations are

$$\left[\mathbb{C}\left(\nabla^S \mathbf{u}^h\right)\mathbf{n} - \mathbf{t}\right](\tau_{kl}) = \mathbf{0} \qquad \tau_{kl} \subset \text{edge} \subset \Gamma_c \tag{43}$$

i.e., they are the collocated strong form of the equilibrium bcs involving the contact pressures at τ_{kl} and differ from eq. (24) simply by the substitution of the known pressure $\mathbf{p}$ with the contact traction $\mathbf{t}$ given by eq. (42). At collocation points located within the inactive contact

boundary, $\mathbf{t}$ vanishes and homogeneous Neumann bcs are automatically recovered. At corners between contact boundaries, equations such as (25) are written with $\mathbf{t}'$ and $\mathbf{t}''$ in place of $\mathbf{p}'$ and $\mathbf{p}''$. In case of inactive contact, one or both of the contact tractions vanish, so that the corresponding contact constraints are automatically replaced by homogeneous Neumann bcs.

The contact equations for the HC and BC methods can once again be simply obtained from eqs. (26) (or (27)) and (28), respectively, by substituting for the pressure $\mathbf{p}$ the contact traction $\mathbf{t}$, and read

$$\int_{\Omega} \left[\mathrm{div}\left(\mathbb{C}\nabla^S \mathbf{u}^h\right) + \mathbf{f}\right] R^b d\Omega - \int_{\Gamma_{p\bar{k}}} \left[\mathbb{C}\left(\nabla^S \mathbf{u}^h\right)\mathbf{n}_{\bar{k}} - \mathbf{t}_{\bar{k}}\right] R^b d\Gamma = \mathbf{0} \qquad \tau_{kl} \subset \text{edge} \subset \Gamma_c \tag{44}$$

$$\left[\mathrm{div}\left(\mathbb{C}\nabla^S \mathbf{u}^h\right) + \mathbf{f}\right](\tau_{kl}) - \frac{C^*}{h}\left[\mathbb{C}\left(\nabla^S \mathbf{u}^h\right)\mathbf{n} - \mathbf{t}\right](\tau_{kl}) = \mathbf{0} \qquad \tau_{kl} \subset \text{edge} \subset \Gamma_c \tag{45}$$

5.4 Enforcement of contact constraints with Nitsche's method

The so-called Nitsche's method differs from the penalty method for the presence of the consistency term in the expression of the contact traction, as follows:

$$\mathbf{t} = \mathbb{C}\left(\nabla^S \mathbf{u}^h\right)\mathbf{n} - \varepsilon_N g_N \bar{\mathbf{n}}^{(m)} \tag{46}$$

Unlike eq. (42), eq. (46) is consistent as the gap tends to zero. With the BC method, inserting eq. (46) into eq. (43) leads to the enforcement of the contact constraints in the form of Dirichlet bcs, by imposing that the gap vanishes at all collocation points on the (active) contact boundary. Insertion of eq. (46) into eqs. (26) (or (27)) and (28) delivers Nitsche's contact conditions for the HC and EC methods, respectively:

$$\int_{\Omega} \left[\mathrm{div}\left(\mathbb{C}\nabla^S \mathbf{u}^h\right) + \mathbf{f}\right] R^b d\Omega - \int_{\Gamma_{p\bar{k}}} \varepsilon_N g_N \bar{\mathbf{n}}^{(m)} R^b d\Gamma = \mathbf{0} \qquad \tau_{kl} \subset \text{edge} \subset \Gamma_c \tag{47}$$

$$\left[\mathrm{div}\left(\mathbb{C}\nabla^S \mathbf{u}^h\right) + \mathbf{f}\right](\tau_{kl}) - \frac{C^*}{h}\left(\varepsilon_N g_N \bar{\mathbf{n}}^{(m)}\right)(\tau_{kl}) = \mathbf{0} \qquad \tau_{kl} \subset \text{edge} \subset \Gamma_c \tag{48}$$

The implementation of Nitsche's method is thus clearly straightforward in the collocation framework, as the consistency term cancels out within the strong form of the boundary equations. Conversely, its implementation within the Galerkin framework is quite cumbersome as it requires the evaluation of additional boundary integrals. The use of Nitsche's method is not further investigated here and will be pursued by the authors in future research.

5.5 The two-half-pass algorithm

In the classical Galerkin setting, contact constraints are usually enforced by considering one of the contacting surfaces as slave and the other one as master. In order to determine the active contact boundary, i.e. the portion of the surfaces where penetration between the bodies takes place, a loop is performed over the discretized slave surface, the values of the gap are evaluated according to eq. (36), and an active contact status flag is assigned to the surface regions where $g_N \leq 0$. Evaluation of the gap and the corresponding enforcement of the non-penetration constraint may take place at the nodes (such as in the classical node-to-surface formulation largely used in conjunction with linear elements, see Zavarise and De Lorenzis 2009, and recently extended to the isogeometric setting by Matzen and Bischoff 2013), or at Gauss-Legendre quadrature points located on the contact surface (such as in the formulation proposed by Fischer and Wriggers 2005 and extended to the isogeometric setting by Temizer et al. 2011, De Lorenzis et al. 2011 and Dimitri et al. 2014). More complex formulations within the framework of mortar methods evaluate the gap at the contact quadrature points and then project their values onto the nodes or control points where the contact constraints are enforced (see, e.g., Puso and Laursen 2004, and the isogeometric extension by Temizer et al. 2012 and De Lorenzis et al. 2012).

Despite the different way the contact contribution is introduced into the variational framework and discretized, all these formulations share two main features which are relevant to the present discussion: a) they introduce a bias between the slave and the master surfaces, as they prevent the slave body from penetrating into the master body but not vice versa; b) they enforce *a priori* the local pressure equilibrium between the contacting bodies. The latter is the main reason why these formulations do not seem to fit well into the collocation framework. Should one of the contacting surfaces be chosen as slave, the gap would need to be evaluated and the

contact constraints enforced at all collocation points located on the slave surface. The contact traction $\mathbf{t}$ would thus be computed on the slave surface, and due to the *a priori* enforcement of equilibrium the opposite traction $-\mathbf{t}$ would need to be applied to the master surface. However, this transfer would not be obvious to realize for meshes with non-matching locations of the collocation points on the contacting surfaces. The same transfer does not represent any problem within a weak formulation in the Galerkin setting, however, the bias between the two surfaces still remains.

Sauer and De Lorenzis (2013) proposed an alternative approach which they called the "two-half-pass formulation", as opposed to the classical procedure termed "full-pass". A similar formulation had been proposed in earlier works by Papadopoulos and co-workers (Papadopoulos et al. 1995). In this approach, two loops are performed treating each surface alternatively as slave and master. In each loop ("half-pass"), the contact tractions are computed only on the surface currently treated as slave. Therefore, no transfer of tractions to the master side is needed. Local equilibrium at the surfaces is not enforced *a priori* but has been shown to be recovered with high accuracy. The advantages of the two-half-pass approach are the unbiased treatment of both surfaces as well as an increased degree of robustness observed within the Galerkin setting.

The two-half-pass formulation is adopted herein to address the enforcement of contact constraints within the collocation framework. These constraints are enforced at the collocation points situated on the contacting surfaces. During each half-pass, one of the potentially contacting surfaces is treated as slave. At each collocation point on this surface, the gap and the contact traction are computed using eqs. (36) and (42), respectively. The latter is then used within eqs. (43), (44) or (45), depending on the specific method used. Note that these are all non-linear equations, since $\mathbf{t}$ as given by eq. (42) is evaluated in the current configuration. This implies that, in the computation of the gap from eq. (36), the projection point $\bar{\mathbf{x}}^{(m)}$ of each slave collocation point and the corresponding normal $\bar{\mathbf{n}}^{(m)}$ are both let to vary, so that the contact traction is a non-linear function of the unknown displacements. Eqs. (43), (44) or (45) are here consistently linearized (see the Appendix) and the problem is solved using the classical Newton-Raphson iterative procedure.

6 Examples on contact

In this section, some examples are presented to illustrate the performance of the contact formulation described in the previous section. The first two examples deal with contact between a deformable body and a rigid obstacle. They include the Hertz problem, a classical benchmark due to the availability of an analytical solution, and a rigid indentor problem. The next two examples tackle contact between two deformable bodies using the two-half-pass formulation. The third example is the so-called contact patch test, often used to evaluate the capability of a contact formulation to transfer uniform stresses across the contact surfaces and thus to converge to the exact solution in the presence of non-conforming discretizations. The fourth example involves contact between two deformable blocks. In most of the examples, the effect of mesh non-uniformity is investigated in light of the observations made for Neumann bcs. As HC has been shown in Section 4 to deliver inferior results as compared to EC, and also because of its higher computational cost, the comparisons in this section are limited to BC and EC. In the latter case, the value of $C^* = 4$ as identified in Section 4 is used. In the last three examples, results are only reported for $p_1 = p_2 = 2$ but higher-order interpolations lead to similar conclusions.

6.1 Example C1: the Hertz problem

The first contact example deals with frictionless contact of a cylinder of radius $R = 1$ on a rigid plane, see Figure 17. The material of the cylinder is linearly elastic with Lamé constants $\mu = 0.5$ and $\lambda = 1.0$, corresponding to Young's modulus $E = 1.333$ and Poisson's ratio $\nu = 0.333$. The cylinder is loaded with a vertical force $P = 0.0048$ applied as a uniformly distributed load on the upper surface. Symmetry restraints are placed on the vertical axis in order to prevent rigid body motion. Although this setup does not correspond exactly to the original Hertz model, the related error is negligible provided that the applied load is sufficiently small. Hertz theory gives in this case $a = 0.0641$, a being the half-width of the contact area. The penalty parameter is $\varepsilon_N = 10^3$. Three different meshes are considered to evaluate the effect of mesh refinement on results. In all cases, the mesh is refined close to the contact region by using non-uniform knot vectors, see Figure 18. In all meshes, the chosen amount of redistribution of the knot vector

entries is such that 85% of the elements are located within 20% of the total length of the knot vector.

The contact tractions obtained from the BC approach at all collocation points ($p = t_N = -\varepsilon_N g_N$ as per eq. (42)) with linear (for simplicity) intermediate interpolation are shown in Figures 19 to 21. Note that the tractions are normalized with respect to the maximum value obtained in the center of the contact area. Results show a satisfactory agreement with the analytical solution and display a monotonic improvement of the pressure distribution quality with increasing resolution at a fixed order. For a given resolution, the quality of the contact pressure distribution is virtually unaffected by the order. This result was already obtained for NURBS discretizations in a Galerkin framework (see Temizer et al. 2011, 2012, and De Lorenzis et al. 2011, 2012) and is in contrast with the observations made for higher-order Lagrange elements, where the contact stresses feature oscillations at the boundary between active and inactive contact regions, whose magnitude increases with the discretization order.

In order to evaluate the effect of the mesh aspect ratio on the accuracy of the contact stress distributions, further analyses are performed by using a 150x30 control net with a uniform knot vector in the radial direction and a non-uniform knot vector in the circumferential direction, such that 85% of the elements are located within 10% of the total length of the knot vector. This leads to a distance between adjacent collocation points which is larger in the radial direction, i.e. in the direction perpendicular to the lower edge of the cylinder where either contact constraints or homogeneous Neumann bcs are enforced. As shown earlier, this is the most critical condition for the accuracy of the solution in the vicinity of this edge. Figure 22 illustrates that, close to the boundary between contact and no-contact regions, for the same non-uniform discretization, EC delivers a more accurate contact pressure distribution than BC. Note that, in all cases, contact pressures are greater than or equal to zero *pointwise*, which is a priori guaranteed by BC and EC. This is a property not satisfied by classical Lagrange finite elements.

6.2 Example C2: the rigid indentor

In the second contact example, a deformable block with Lamé constants $\mu = 0.5$ and $\lambda = 0.8$ is pressed against a rigid indentor of smaller width by imposing a uniform vertical displacement $\bar{v} = 0.3$ (along with zero horizontal displacement) to its upper edge. The penalty parameter is

$\varepsilon_N = 10^3$. The problem geometry is illustrated in Figure 23, where the locations of the Greville collocation points for the two investigated meshes are reported. In both cases, the distance between adjacent collocation points is larger in the direction perpendicular to the lower edge. As demonstrated earlier, this corresponds to the most critical case for this portion of the boundary, where either contact constraints or homogeneous Neumann bcs are enforced.

Figures 24a and b illustrate the BC results for the two meshes. With mesh 2, no iterative convergence is obtained due to large oscillations of the solution in the vicinity of the corner of the indentor. The deformed shape reported in Figure 24b corresponds to the unconverged state after the 10th iteration. The oscillations of the solution lead to loss of convergence of the active set algorithm, which in turns leads to failure of the iterative procedure. The residual norm oscillates indefinitely between three values, which correspond to the three deformed shapes shown as close-ups in Figures 25a-c. It is evident that these three configurations correspond to three different active sets. Conversely, the EC formulation achieves iterative convergence for both meshes by preventing the strong local oscillations. The solution for mesh 2 is shown in Figure 24d whereas a close-up of the corner region is given in Figure 25d. Here the active set is different from any of the three unconverged active sets obtained with BC, and remains stable so that convergence is achieved in one iteration. We are well aware that the large rotations and strains about the corner of the rigid indentor are not consistent with the use of small deformation linear elasticity. However, we only intend this problem as a severe test of the contact formulations, which fully account for large geometric changes.

6.3 Example C3: the contact patch test

The contact patch test, proposed by Taylor and Papadopoulos (1991), is classically adopted in contact mechanics to test the capability of a contact formulation to transfer a constant contact pressure across the interface between discretized bodies with non-conforming meshes. This is viewed as a necessary condition for convergence to the exact solution upon mesh refinement. Among the most widely used contact formulations within the Galerkin framework, the node-to-surface (NTS) algorithm is known to fail the contact patch test, as the local enforcement of the non-penetration condition at the slave nodes leads to local violation of the equilibrium of moments at the contact interfaces (Zavarise and De Lorenzis 2009); mortar algorithms pass

the contact patch test to machine precision, as a result of their non-local enforcement of the contact constraints; Gauss-point-to-surface (GPTS) approaches (Fischer and Wriggers 2005, see also Dimitri et al. 2014), whereby the enforcement of the contact constraints occurs at multiple locations within each slave contact surface element, pass the contact patch test to within the integration error of the contact contribution to the weak form. Sauer and De Lorenzis (2013) showed that the two-half-pass version of the GPTS approach passes the contact patch test to machine precision for low or moderate penalty parameters.

Figure 26 illustrates the geometry of the contact patch test adopted herein. The two blocks have Lamé constants $\mu = 0.5$ and $\lambda = 1.0$, and are pressed onto each other with a uniform pressure $\bar{p} = 0.1$ applied in 10 loading steps. Symmetry bcs are enforced on the left vertical edges of both blocks. In all points of the lower edge of the lower block, zero vertical displacement and zero shear stress are imposed. Figure 27a,b shows the vertical displacement contour on the deformed geometry and the relative error of the stress σ_y (with respect to the exact solution equal to $-\bar{p}$) obtained with the BC approach for a penalty parameter $\varepsilon_N = 10$. A visible penetration error is observed in Figure 27a due to the low value of the penalty parameter. Nevertheless, the exact stress solution is attained within machine precision. In Figure 27c,d, the penalty parameter is raised to $\varepsilon_N = 100$, which obviously leads to smaller (now visually imperceptible) penetrations (Figure 27c). The error in the stress computation is still at machine precision 27d. Thus, interestingly, the collocation approach does pass the contact patch test despite its local enforcement of the contact constraints at the collocation points. The reason is that the governing equations involve contact *pressures*. Conversely, in the NTS approach, where the contact constraints are also enforced locally at the slave nodes, the contact residual contributions are computed in the form of *concentrated forces* at the slave nodes, and a uniform smearing of these forces over the contact elements (Zavarise and De Lorenzis 2009) is not sufficient for an accurate recovery of the contact pressure distribution.

Note that in this example, as the exact solution features uniform deformation and stress states throughout the blocks, the BC and EC approaches (as well as the HC one) deliver identical results regardless of the aspect ratio of the employed mesh.

6.4 Example C4: the two deformable blocks

In this example, a deformable block with Lamé constants $\mu = 0.5$ and $\lambda = 0.5$ is pressed against another deformable block with the same elastic constants but larger width, by imposing a uniform vertical displacement $\bar{v} = 0.2$ (along with zero horizontal displacement) to its upper edge in 20 time steps. The lower edge of the lower block is restrained against both vertical and horizontal displacements. Once again, we are fully aware that the large deformations of the blocks are not consistent with the use of linear elasticity. However, we simply view this as a severe test of the contact formulation which is applicable to large deformations.

The penalty parameter is set to $\varepsilon_N = 1500$. This large value is needed to prevent visible penetrations at the corners of the upper block where large stress concentrations are expected. The problem geometry is illustrated in Figure 28, where the locations of the Greville collocation points for the first two investigated meshes are reported. In mesh 1, the distance between adjacent collocation points is similar in both horizontal and vertical directions. In the second mesh, this distance is larger in the horizontal direction, i.e. in the direction perpendicular to the vertical edges of the blocks where homogeneous Neumann bcs are enforced. As demonstrated earlier, this corresponds to the most critical case for this portion of the boundary.

Figure 29a,b illustrate the BC results for the two meshes in terms of σ_y stress contours. The expected large stress concentrations at the corners of the blocks are correctly captured with mesh 1, whereas mesh 2 leads to spurious stress oscillations of significant magnitude. These are due to the strong enforcement of the Neumann bcs on the vertical edges of both blocks, and are consistent with observations in earlier examples. The oscillations disappear when using the EC formulation, which leads to the expected solution for both meshes (Figure 29c,d).

Additional meshes are investigated where the distance between adjacent collocation points is larger in the vertical direction, i.e. in the direction perpendicular to the horizontal edges of the blocks where the contact constraints (or, for the inactive contact regions, homogeneous Neumann bcs) are enforced. This thus corresponds to the most critical case for this portion of the boundary. When using the BC formulation, the iterative procedure fails at loading step 7 for a mesh with 25x5 control points, and at loading step 18 for a mesh with 20x5 control points. As already observed in the rigid indentor example, the loss of iterative convergence is

due to failure of the active set algorithm, in turn due to strong local oscillations of the solution taking place in the vicinity of the contact boundary. By suppressing these oscillations, the EC formulation achieves convergence for both meshes. The mesh with 25x5 control points and the corresponding solution are respectively shown in Figure 30a,b.

7 Conclusions

This paper tackled two important aspects in the development of isogeometric collocation, namely, the imposition of Neumann bcs, and the enforcement of contact constraints between multiple patches with non-conforming discretizations. Both issues fit into the same framework as contact constraints can be viewed as a special type of Neumann bc. Notably, contact is the first non-linear solid mechanics problem for which isogeometric collocation is investigated. This paper tackled frictionless contact, but the extension to the frictional case is conceptually straightforward and is currently underway. The following main conclusions were reached:

- for problems featuring reduced regularity of the solution (e.g., problems with incompatible bcs at corners) and non-uniform meshes, the strong imposition of Neumann bcs in the conventional collocation method may lead to a significant loss of accuracy;

- in such situations, the proposed enhanced collocation scheme, whereby the Neumann bcs are imposed considering both boundary and bulk contributions, significantly improves the accuracy over the conventional collocation method and achieves an accuracy comparable to that of the Galerkin method, especially for discretizations of order larger than 3, while completely eliminating quadrature. The penalty-like constant required by this approach was calibrated for small-deformation elasticity and is expected to be operator-dependent but not problem-dependent;

- the proposed hybrid collocation-Galerkin scheme is also effective in improving the accuracy, especially for high discretization orders. In comparison to the enhanced collocation scheme, this method has the disadvantage of requiring computation of a boundary integral, but the advantage that it contains no penalty-like constant in need of calibration;

- for contact problems between deformable bodies, the two-half-pass formulation seems the most natural algorithm in the collocation framework. Despite the pointwise evaluation of the contact residual contributions at the surface collocation points, the formulation passes the contact patch test to machine precision;

- the proposed frictionless contact formulation in the collocation setting yields results of very good quality for regular solutions and uniform meshes. In situations with highly non-uniform meshes, as for the more general Neumann cases, the original collocation method fails whereas the proposed enhanced collocation scheme is an effective remedy which restores accuracy of the results and robustness of the iterative procedure.

8 Acknowledgments

L. De Lorenzis and A. Reali have received funding for this research from the European Research Council under the European Union's Seventh Framework Programme (FP7/2007-2013) / ERC Grant agreements n° 279439 (L. De Lorenzis) and n° 259229 (A. Reali). T.J.R. Hughes and J.A. Evans were supported by grants from the Office of Naval Research (N00014-08-1-0992), the National Science Foundation (CMMI-01101007) and SINTEF (UTA10-000374), with the University of Texas at Austin.

References

[1] N.R. Aluru. A point collocation method based on reproducing kernel approximation. International Journal for Numerical Methods in Engineering, 47:1083–1121, 2000.

[2] F. Auricchio, L. Beirão da Veiga, T.J.R. Hughes, A. Reali, and G. Sangalli. Isogeometric collocation methods. Mathematical Models and Methods in Applied Sciences, 20(11):2075–1077, 2010.

[3] F. Auricchio, F. Calabrò, T.J.R. Hughes, A. Reali, and G. Sangalli. A simple algorithm for obtaining nearly optimal quadrature rules for NURBS-based isogeometric analysis. Computer Methods in Applied Mechanics and Engineering, 249–252:15–27, 2012a.

[4] F. Auricchio, L. Beirão da Veiga, T.J.R. Hughes, A. Reali, and G. Sangalli. Isogeometric collocation for elastostatics and explicit dynamics. Computer Methods in Applied Mechanics and Engineering, 249–252:2–14, 2012b.

[5] F. Auricchio, L. Beirão da Veiga, J. Kiendl, C. Lovadina, and A. Reali. Locking-free isogeometric collocation methods for spatial Timoshenko rods. Computer Methods in Applied Mechanics and Engineering, 263:113-126, 2013.

[6] L. Beirão da Veiga, C. Lovadina, and A. Reali. Avoiding shear locking for the Timoshenko beam problem via isogeometric collocation methods. Computer Methods in Applied Mechanics and Engineering, 241–244:38–51, 2012.

[7] M. Bischoff, W.A. Wall, K.-U. Bletzinger, and E. Ramm. Models and Finite Elements for Thin-walled Structures. In E. Stein, R. de Borst, and T.J.R. Hughes, editors, Encyclopedia of Computational Mechanics, 2(3):59–137. John Wiley & Sons, 2004.

[8] S.W. Chi, J.S. Chen, H.Y. Hu, and J.P. Yang. A gradient reproducing kernel collocation method for boundary value problems, International Journal for Numerical Methods in Engineering, 93:1381–1402, 2013.

[9] J.A. Cottrell, T.J.R. Hughes, and Y. Bazilevs. Isogeometric analysis: Toward Integration of CAD and FEA. John Wiley & Sons, 2009.

[10] L. De Lorenzis, I. Temizer, P. Wriggers, and G. Zavarise. A large deformation frictional contact formulation using NURBS-based isogeometric analysis. International Journal for Numerical Methods in Engineering, 87(13):1278-1300, 2011.

[11] L. De Lorenzis, P. Wriggers, and G. Zavarise. A mortar formulation for 3D large deformation contact using NURBS-based isogeometric analysis and the augmented Lagrangian method. Computational Mechanics, 49(1):1-20, 2012.

[12] R. Dimitri, L. De Lorenzis, M.A. Scott, P. Wriggers, R.L. Taylor, and G. Zavarise. Isogeometric large deformation frictionless contact using T-splines. Computer Methods in Applied Mechanics and Engineering, 269:394-414, 2014.

[13] J.A. Evans, Y. Bazilevs, I. Babuška, and T.J.R. Hughes. n-widths, sup-infs, and optimality ratios for the k-version of the isogeometric finite element method. Computer Methods in Applied Mechanics and Engineering, 198(21–26):1726–1741, 2009.

[14] K. A. Fischer, and P. Wriggers. Frictionless 2D contact formulations for finite deformations based on the mortar method. Computational Mechanics, 36:226–244, 2005.

[15] P. Grisvard. Problemes aux limites dans les polygones. Mode d'emploi, Bull. Dir, Etud. Rech., Ser, C, No. 1, 1986.

[16] P. Grisvard. Elliptic Problems in Nonsmooth Domains. Society for Industrial and Applied Mathematics, 425 pp., 2011.

[17] D. Großmann, B. Jüttler, H. Schlusnus, J. Barner, and A.H. Vuong. Isogeometric simulation of turbine blades for aircraft engines. Computer Aided Geometric Design, 29(7):519–531, 2012.

[18] H.Y. Hu, J.S. Chen, and W. Hu. Weighted radial basis collocation method for boundary value problems. International Journal for Numerical Methods in Engineering, 69:2736–2757, 2007.

[19] H.Y. Hu, J.S. Chen, and W. Hu. Error analysis of collocation method based on reproducing kernel approximation. Numerical Methods for Partial Differential Equations, 27(3):554–580, 2011.

[20] T.J.R. Hughes, J.A. Cottrell, and Y. Bazilevs. Isogeometric analysis: CAD, finite elements, NURBS, exact geometry and mesh refinement. Computer Methods in Applied Mechanics and Engineering, 194:4135–4195, 2005.

[21] T.J.R. Hughes, A. Reali, and G. Sangalli. Efficient quadrature for NURBS-based isogeometric analysis. Computer Methods in Applied Mechanics and Engineering, 199:301–313, 2010.

[22] D.W. Kim, and Y. Kim. Point collocation methods using the fast moving least-square reproducing kernel approximation. International Journal for Numerical Methods in Engineering, 56:1445–1464, 2003.

[23] T.A. Laursen. Computational Contact and Impact Mechanics. Springer, 2002.

[24] M.E. Matzen, T. Cichosz, and M. Bischoff. A point to segment contact formulation for isogeometric, NURBS based finite elements. Computer Methods in Applied Mechanics and Engineering, 255:27–39, 2013.

[25] V.P. Nguyen, T. Rabczuk, S. Bordas, and M. Duflot. Meshless methods: A review and computer implementation aspects. Mathematics and Computers in Simulation, 79:763-813, 2008.

[26] E. Oñate, S. Idelsohn, O.C. Zienkiewicz, and R.L. Taylor. A finite point method in computational mechanics. Application to convective transport and fluid flow. International Journal for Numerical Methods in Engineering, 39:3839–3866, 1996.

[27] P. Papadopoulos, R.E. Jones, and J.M. Solberg. A novel finite element formulation for frictionless contact problems. International Journal for Numerical Methods in Engineering, 38:2603-2617, 1995.

[28] L. Piegl, and W. Tiller. The NURBS Book. Springer, Berlin Heidelberg New York, 2nd edition, 1996.

[29] M.A. Puso, and T.A. Laursen. A mortar segment-to-segment frictional contact method for large deformations. Computer Methods in Applied Mechanics and Engineering, 193:4891–4913, 2004.

[30] R.A. Sauer, and L. De Lorenzis. A computational contact formulation based on surface potentials. Computer Methods in Applied Mechanics and Engineering, 253:369-395, 2013.

[31] D. Schillinger, J.A. Evans, A. Reali, M.A. Scott, and T.J.R. Hughes. Isogeometric Collocation: Cost Comparison with Galerkin Methods and Extension to Adaptive Hierarchical NURBS Discretizations. Computer Methods in Applied Mechanics and Engineering, 267:170-232, 2013.

[32] R.L. Taylor, and P. Papadopoulos. On a patch test for contact problems in two dimensions. In Computational Methods in Nonlinear Mechanics, Wriggers P, Wanger W (eds). Springer: Berlin, 690–702, 1991.

[33] İ. Temizer, P. Wriggers, and T.J.R. Hughes. Contact treatment in isogeometric analysis with NURBS. Computer Methods in Applied Mechanics and Engineering, 200(9–12):1100–1112, 2011.

[34] İ. Temizer, P. Wriggers, and T.J.R. Hughes. Three-Dimensional Mortar-Based Frictional Contact Treatment in Isogeometric Analysis with NURBS. Computer Methods in Applied Mechanics and Engineering, 209-212:115-128, 2012.

[35] P. Wriggers. Computational Contact Mechanics. Springer, 2006.

[36] G. Zavarise, and L. De Lorenzis. A modified node-to-segment algorithm passing the contact patch test. International Journal for Numerical Methods in Engineering, 79:379–416, 2009.

[37] X. Zhang, X.H. Liu, K.Z. Song, and M.W. Lu. Least-squares collocation meshless method. International Journal for Numerical Methods in Engineering, 51:1089–1100, 2001.

A Consistent linearization

Eqs. (43), (44), and (45), respectively for the BC, HC, and EC collocation approaches, contain in different forms the same boundary residual term

$$\mathbf{R}_{bou} = \mathbb{C}\left(\nabla^S \mathbf{u}\right)\mathbf{n} - \mathbf{t} \tag{A.1}$$

where $\mathbf{t}$ is given by eq. (42). For a more concise notation, the superscript h indicating the discretized displacement field is here omitted. Linearization of this residual gives

$$\Delta\mathbf{R}_{bou} = \mathbb{C}\left[\nabla^S\left(\Delta\mathbf{u}\right)\right]\mathbf{n} - \Delta\mathbf{t} \tag{A.2}$$

with Δ as the symbol for linearized increment. In turn, eq. (42) yields

$$\Delta\mathbf{t} = -\varepsilon_N\left(\Delta g_N \bar{\mathbf{n}}^{(m)} + g_N \Delta\bar{\mathbf{n}}^{(m)}\right) \tag{A.3}$$

where Δg_N and $\Delta\bar{\mathbf{n}}^{(m)}$ are given by (Laursen 2002, Wriggers 2006)

$$\Delta g_N = \left(\Delta\mathbf{x}^{(s)} - \Delta\bar{\mathbf{x}}^{(m)}\right)\cdot\bar{\mathbf{n}}^{(m)} \tag{A.4}$$

and

$$\Delta\bar{\mathbf{n}}^{(m)} = -\frac{1}{\bar{m}_{11}^{(m)}}\left(\Delta\bar{\mathbf{x}}_{,\xi}^{(m)}\cdot\bar{\mathbf{n}}^{(m)} + \bar{k}_{11}^{(m)}\Delta\bar{\xi}^{(m)}\right)\bar{\boldsymbol{\tau}}^{(m)} \tag{A.5}$$

In the latter equation it has been assumed that the master surface is parameterized by the convective coordinates $\xi^{(m)}$, that define the covariant vector $\boldsymbol{\tau}^{(m)} = \mathbf{x}_{,\xi}^{(m)}$ and the metric $m_{11}^{(m)} := \left\|\boldsymbol{\tau}^{(m)}\right\|^2$. The curvature follows from $k_{11}^{(m)} = \mathbf{x}_{,\xi\xi}^{(m)}\cdot\mathbf{n}^{(m)}$, where $\mathbf{n}^{(m)}$ is the normal unit vector to the master surface. Being $\bar{\mathbf{n}}^{(m)}$ the normal to the master surface at the projection point, these quantities are all evaluated at the projection point, and the parametric location of this point must also be linearized. It can be shown that (Laursen 2002, Wriggers 2006)

$$\Delta\bar{\xi}^{(m)} = \frac{1}{\bar{A}_{11}^{(m)}}\left[\left(\Delta\mathbf{x}^{(s)} - \Delta\bar{\mathbf{x}}^{(m)}\right)\cdot\bar{\boldsymbol{\tau}}^{(m)} - g_N\bar{\mathbf{n}}^{(m)}\cdot\Delta\bar{\mathbf{x}}_{,\xi}^{(m)}\right] \tag{A.6}$$

with

$$\bar{A}_{11}^{(m)} = \bar{m}_{11}^{(m)} - g_N\bar{k}_{11}^{(m)} \tag{A.7}$$

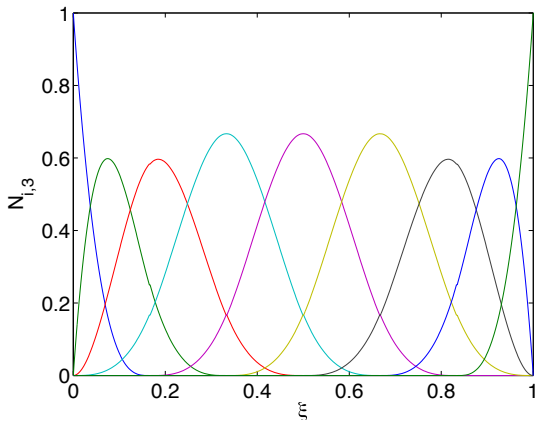

(a)

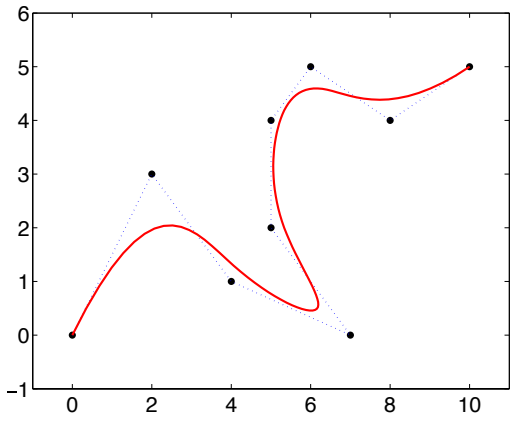

(b)

Figure 1: Example of B-spline basis functions and a corresponding 2D B-spline curve. (a) Cubic B-spline basis functions corresponding to the knot vector $\{0, 0, 0, 0, 1/6, 1/3, 1/2, 2/3, 5/6, 1, 1, 1, 1\}$. (b) A possible 2D B-spline curve generated from the basis functions in (a) by selecting the black points as control points.

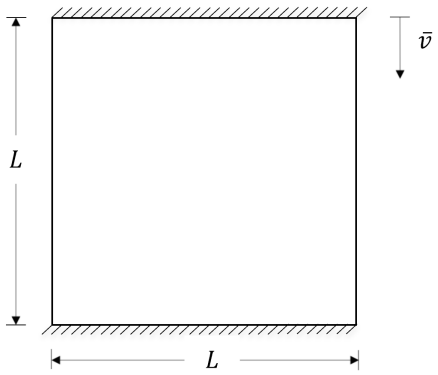

Figure 2: Example N1: the compression test.

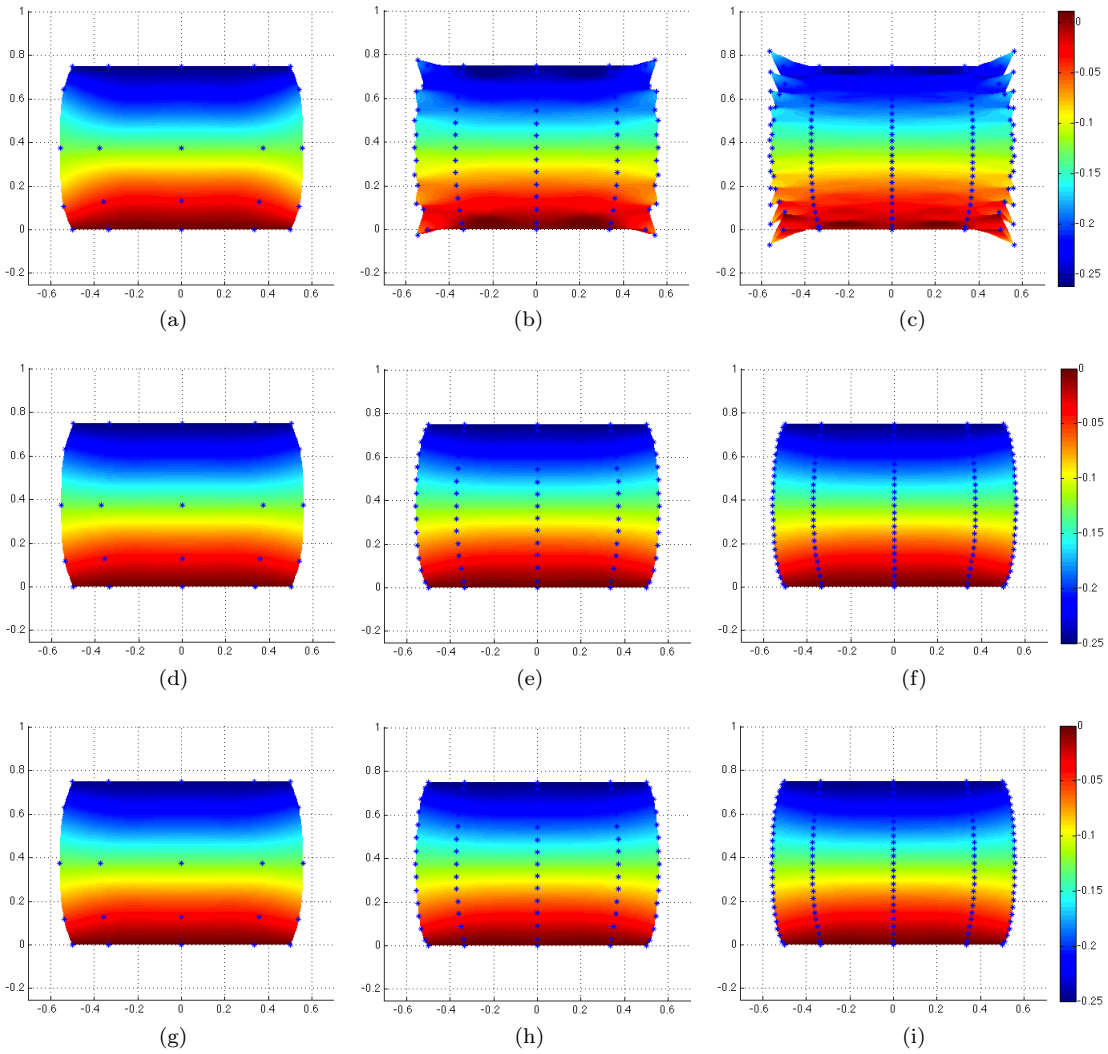

Figure 3: Example N1: results with the BC (a,b,c), HC (d,e,f) and EC (g,h,i) treatments using the Greville abscissae. $p_1 = p_2 = 2$. All contours show the vertical displacement field on the deformed geometry for meshes with 5x5 (a,d,g), 5x15 (b,e,h) and 5x25 (c,f,i) collocation points (aspect ratios of 1, 3, and 5, respectively). In the EC treatment $C^* = 4$. The blue dots represent the Greville collocation points.

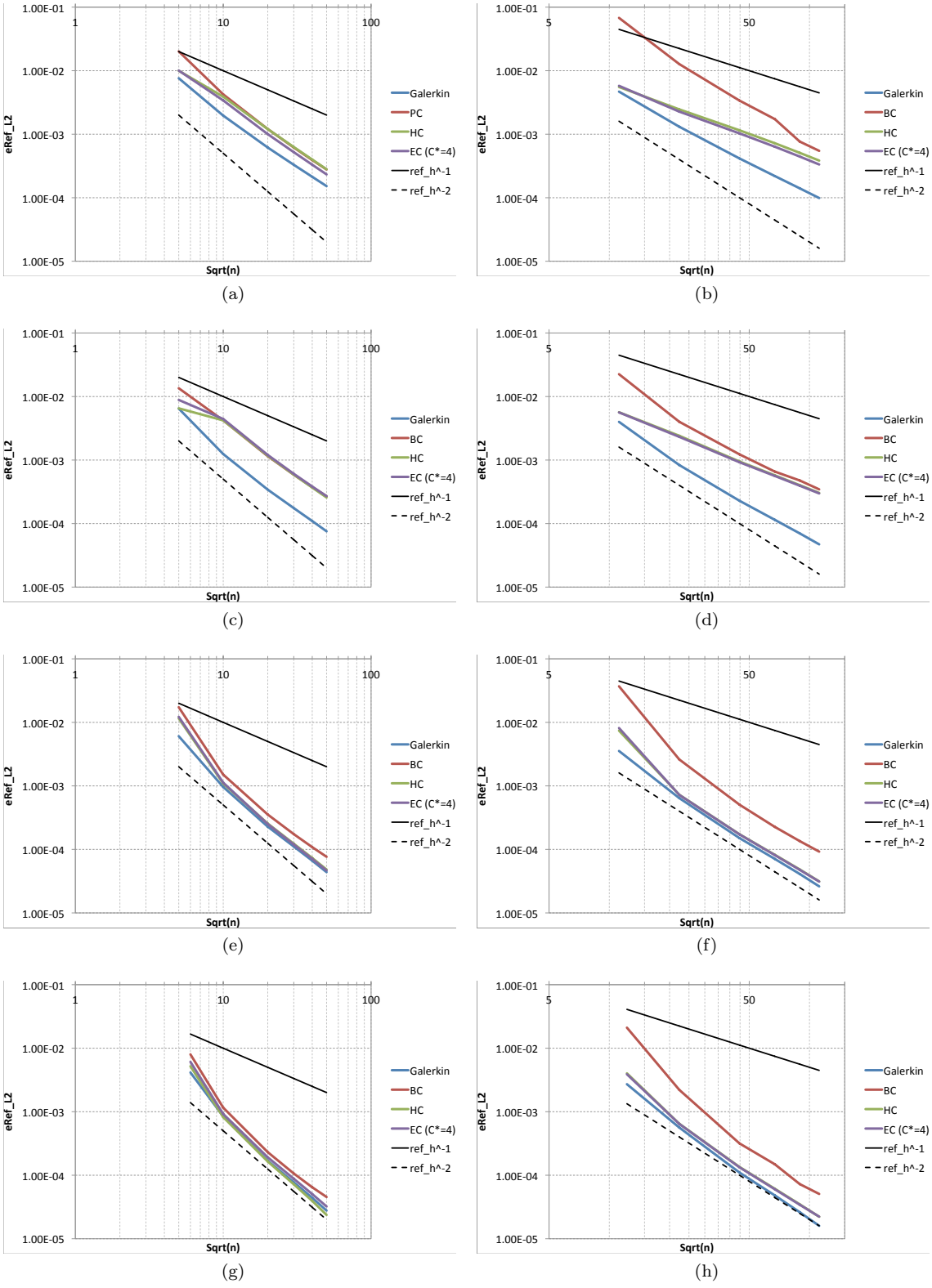

Figure 4: Example N1: displacement error in L_2-norm for a mesh aspect ratio of 1 (a,c,e,g), and 5 (b,d,f,h). $p_1 = p_2 = 2$ (a,b), 3 (c,d), 4 (e,f), 5 (g,h). Collocation is performed at the Greville abscissae.

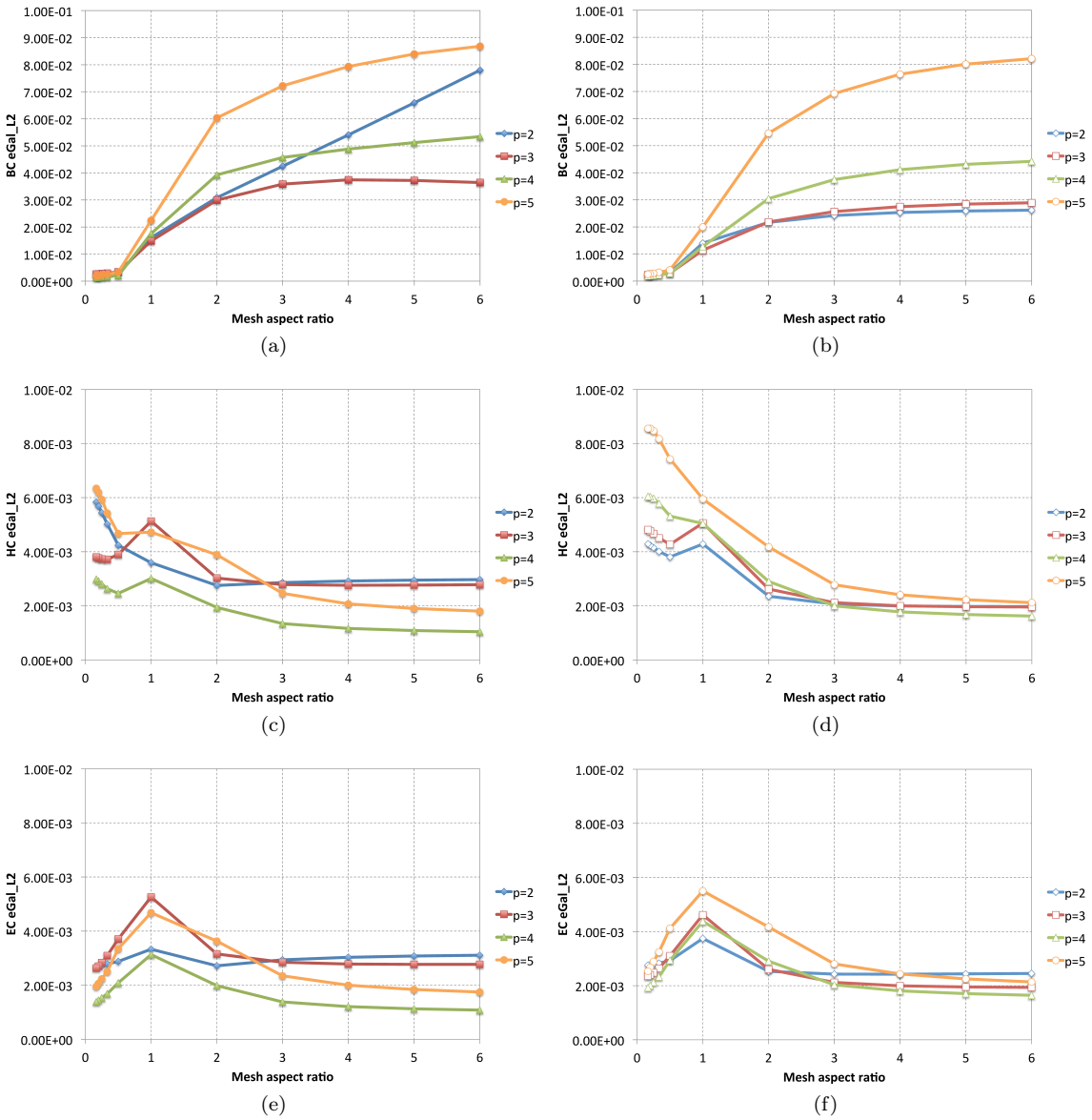

Figure 5: Example N1: comparison between methods. Displacement error in L_2-norm relative to Galerkin results for the same mesh. Collocation is performed at the Greville (a,c,e) and at the Demko (b,d,f) abscissae. The minimum number of control points is fixed to 10 (e.g. an aspect ratio = 3 corresponds to a mesh with 10x30 control points; an aspect ratio of 0.5 corresponds to a mesh with 20x10 control points). In the EC treatment $C^* = 4$.

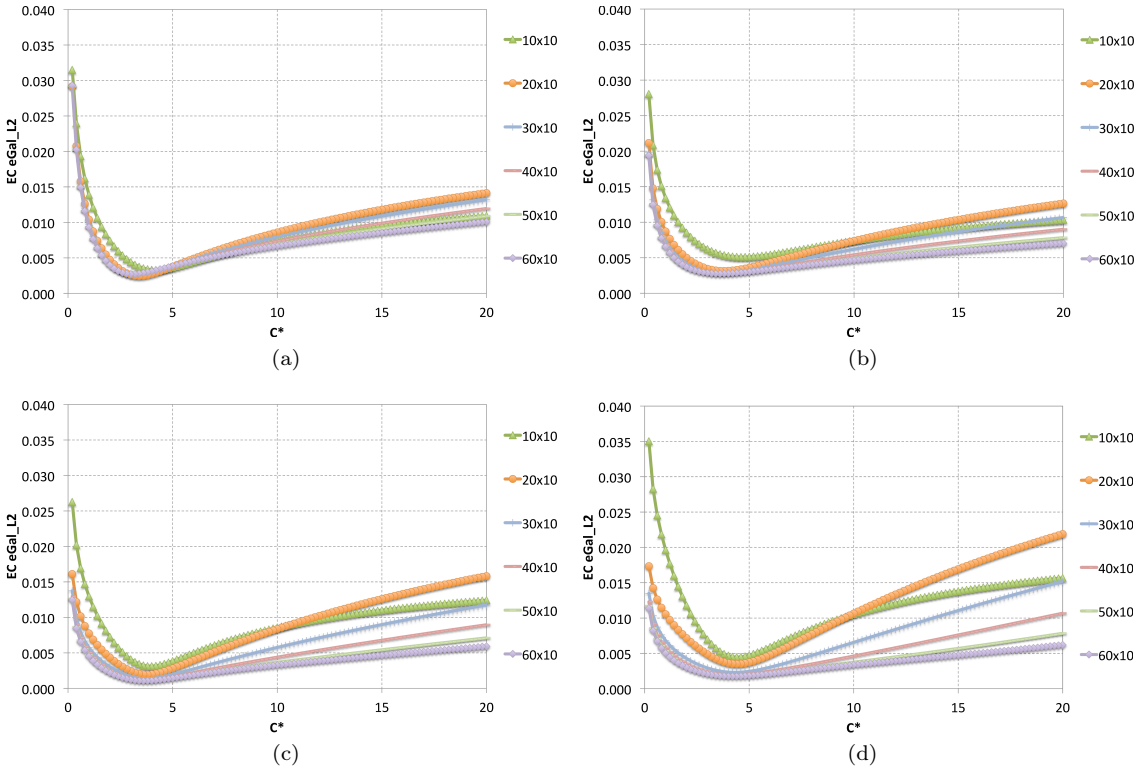

Figure 6: Example N1: displacement error in L_2-norm of the EC treatment relative to Galerkin as a function of C^* using the Greville abscissae and $p_1 = p_2 = 2$ (a), 3 (b), 4 (c), and 5 (d). The minimum number of control points is fixed to 10.

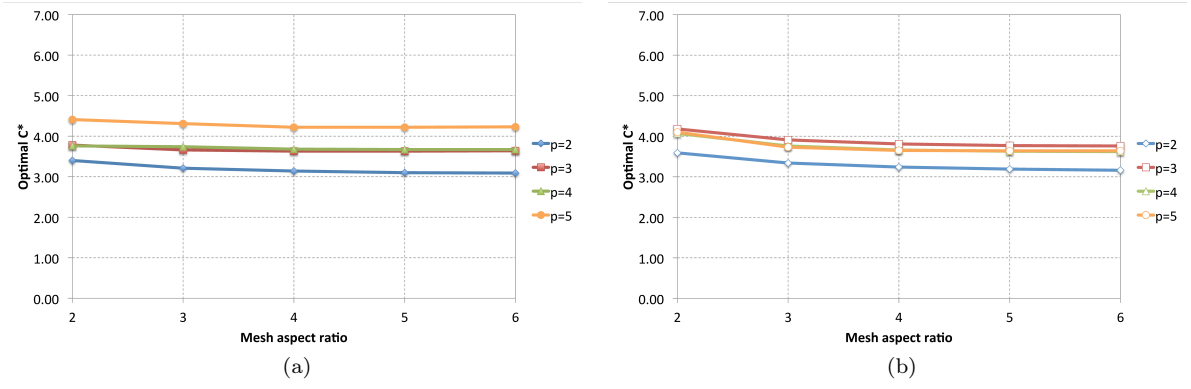

Figure 7: Example N1: optimal C^* versus the mesh aspect ratio using the Greville (a) and Demko (b) abscissae. The minimum number of control points is fixed to 10.

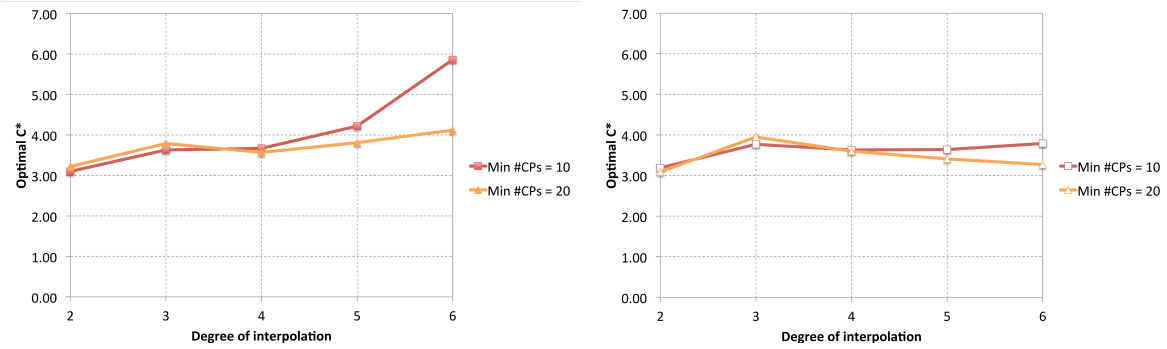

Figure 8: Example N1: optimal C^* for a mesh aspect ratio of 5 versus the degree of interpolation using the Greville (a) and Demko (b) abscissae.

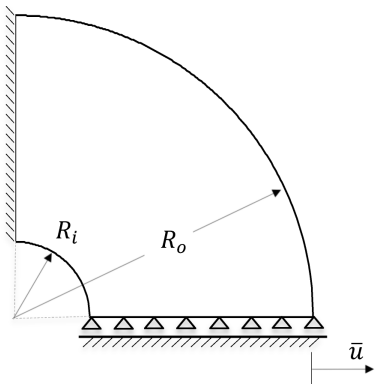

Figure 9: Example N2: the quarter of annulus.

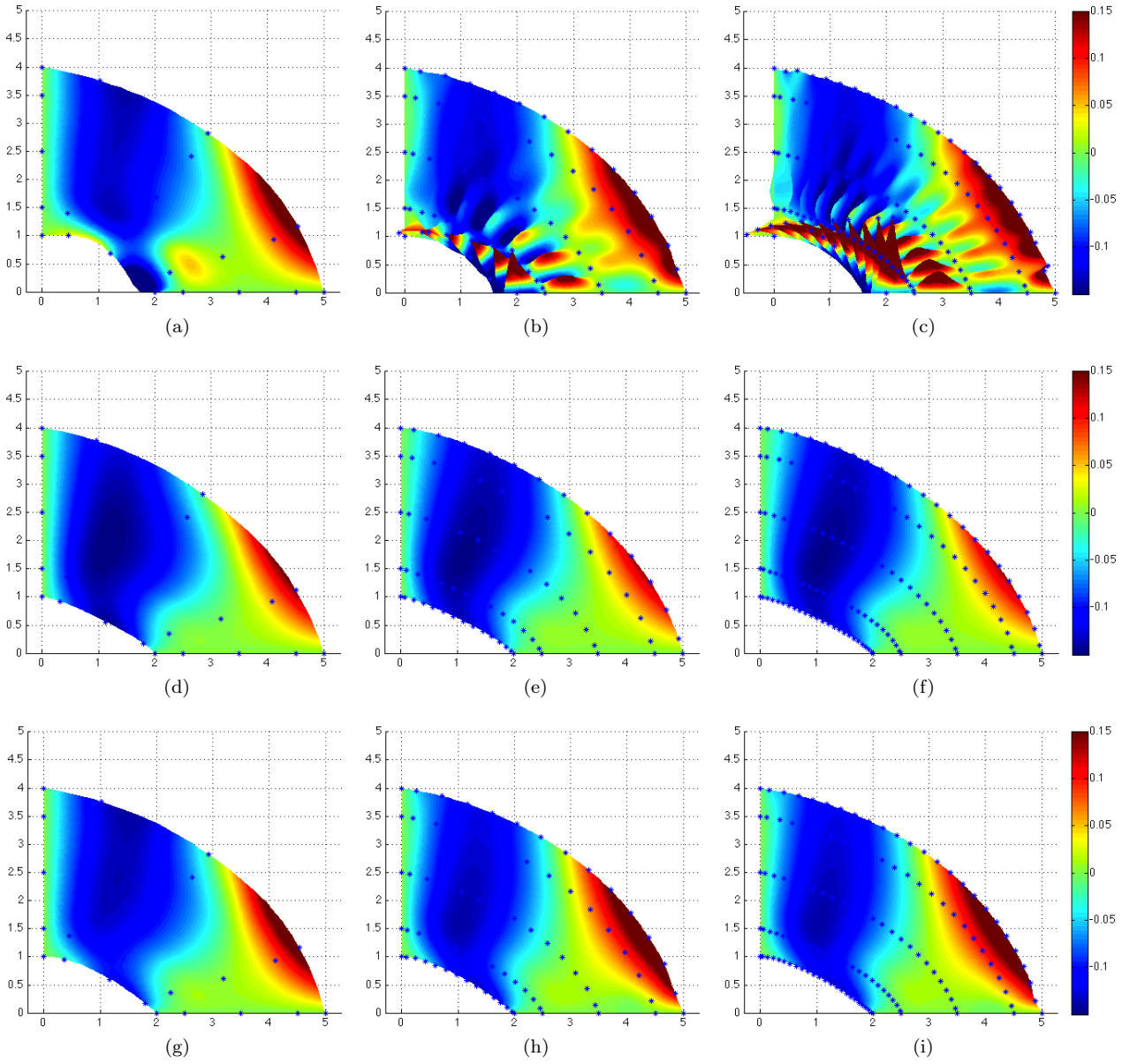

Figure 10: Example N2: results with the BC (a,b,c), HC (d,e,f) and EC (g,h,i) treatments using the Greville abscissae. $p_1 = p_2 = 2$. All contours show the vertical displacement field on the deformed geometry for meshes with 5x5 (a,d,g), 15x5 (b,e,h) and 25x5 (c,f,i) collocation points. In the EC treatment $C^* = 4$. The blue dots represent the Greville collocation points.

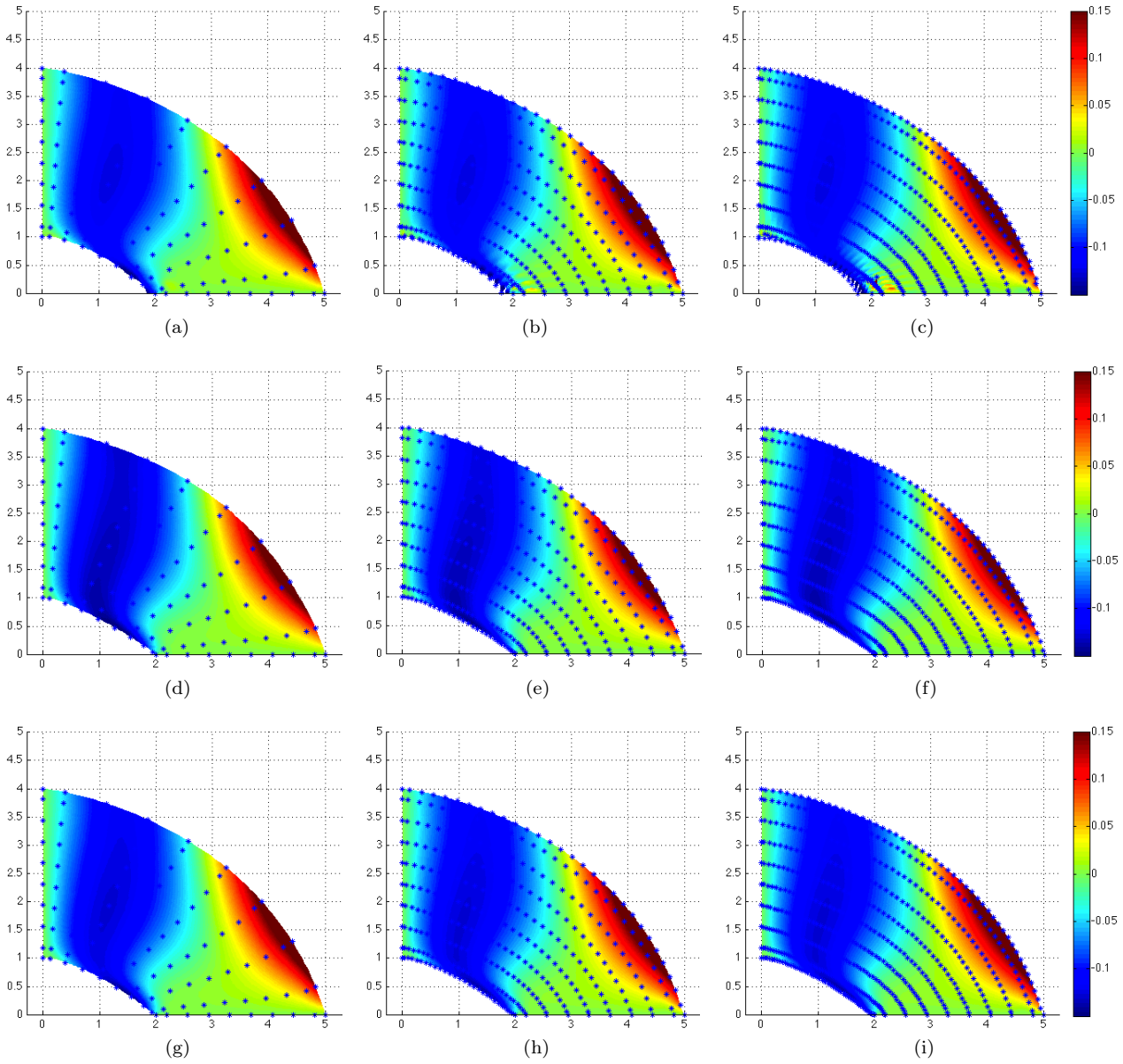

Figure 11: Example N2: results with the BC (a,b,c), HC (d,e,f) and EC (g,h,i) treatments using the Greville abscissae. $p_1 = p_2 = 2$. All contours show the vertical displacement field on the deformed geometry for meshes with 10x10 (a,d,g), 30x10 (b,e,h) and 50x10 (c,f,i) collocation points. In the EC treatment $C^* = 4$. The blue dots represent the Greville collocation points.

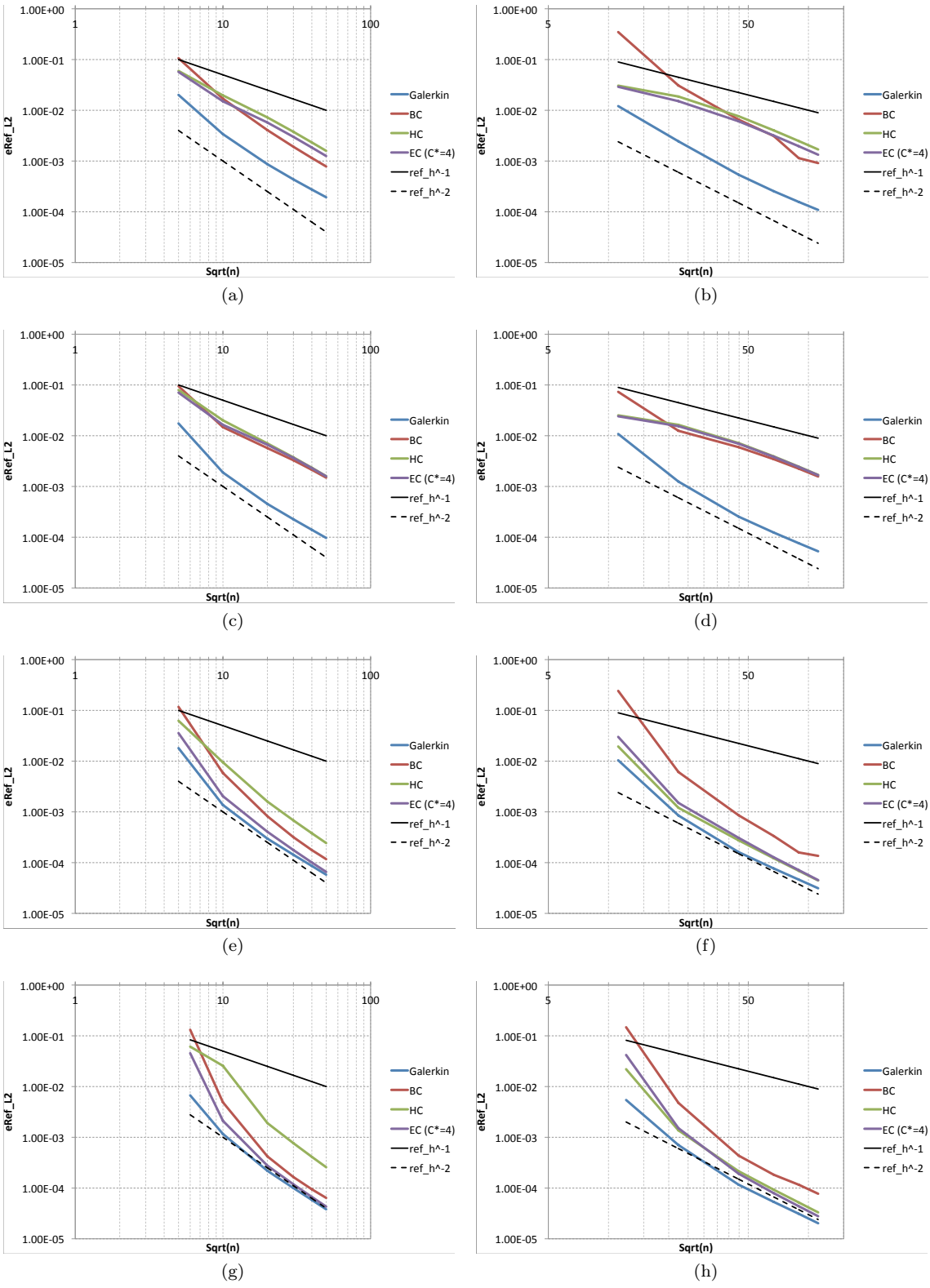

Figure 12: Example N2: displacement error in L_2-norm for a mesh aspect ratio of 1 (a,c,e,g), and 5 (b,d,f,h). $p_1 = p_2 = 2$ (a,b), 3 (c,d), 4 (e,f), 5 (g,h). Collocation is performed at the Greville abscissae.

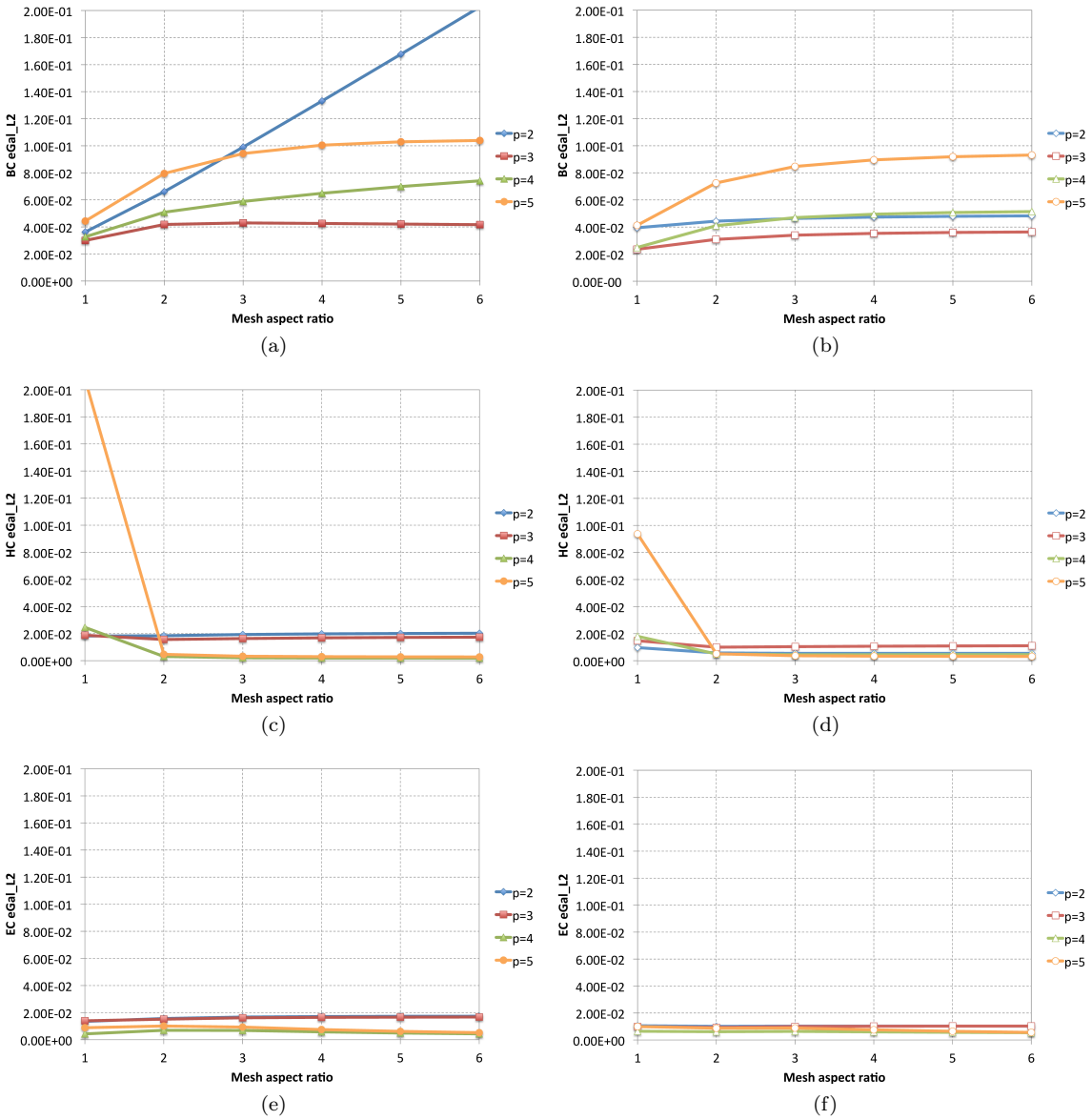

Figure 13: Example N2: comparison between methods. Displacement error in L_2-norm relative to Galerkin results for the same mesh. Collocation is performed at the Greville (a,c,e) and at the Demko (b,d,f) abscissae. The minimum number of control points is fixed to 10 (e.g. an aspect ratio = 3 corresponds to a mesh with 30x10 control points). In the EC treatment $C^* = 4$.

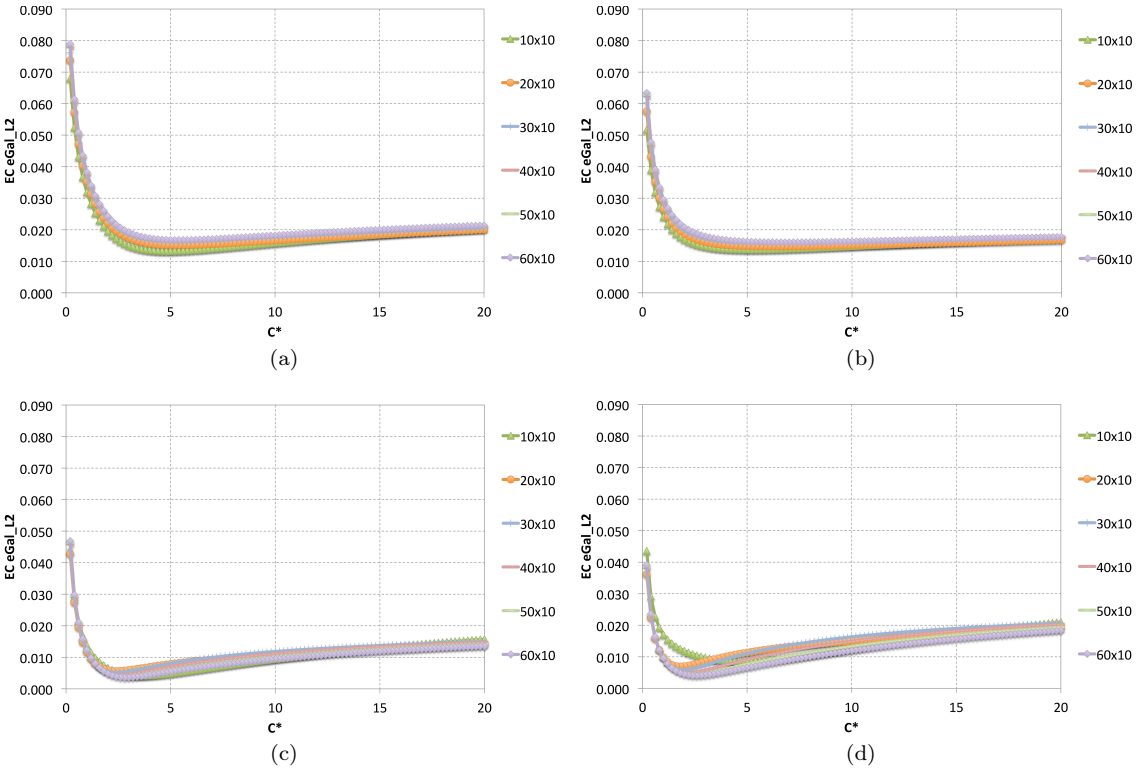

Figure 14: Example N2: displacement error in L_2-norm of the EC treatment relative to Galerkin as a function of C^* using the Greville abscissae and $p_1 = p_2 = 2$ (a), 3 (b), 4 (c), and 5 (d). The minimum number of control points is fixed to 10.

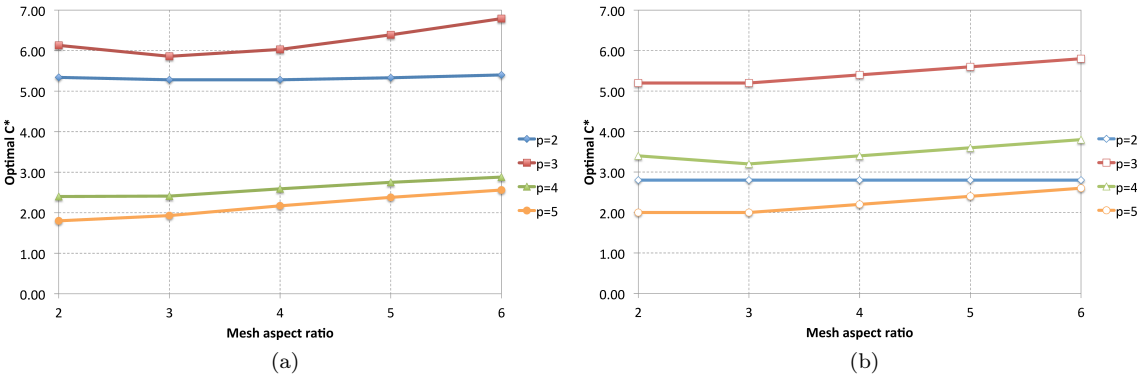

Figure 15: Example N2: optimal C^* versus the mesh aspect ratio using the Greville (a) and Demko (b) abscissae.

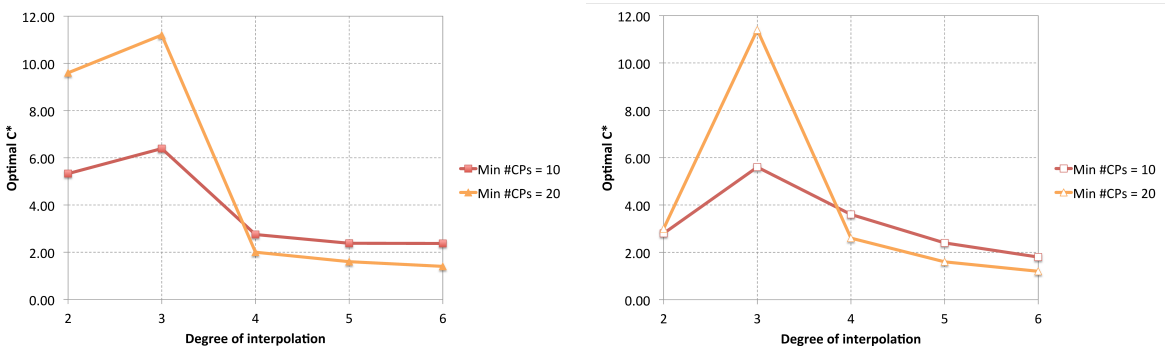

Figure 16: Example N2: optimal C^* versus the degree of interpolation using the Greville (a) and Demko (b) abscissae.

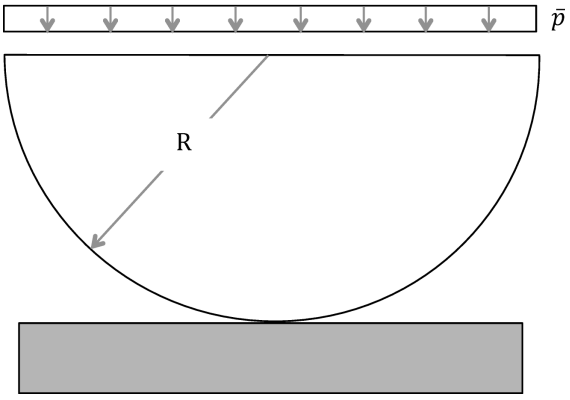

Figure 17: Example C1: the Hertz problem.

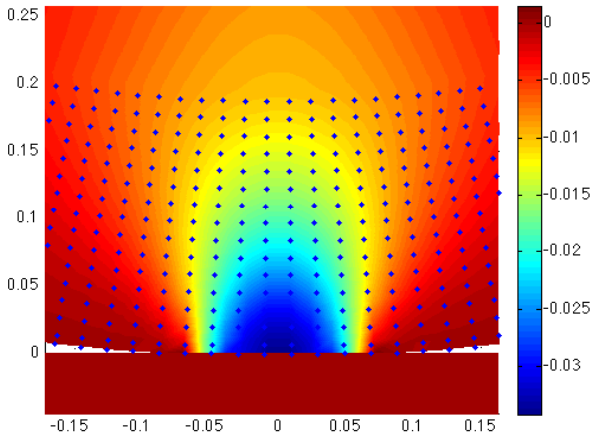

Figure 18: Example C1: contour of stresses σ_y in the vicinity of the contact region. The BC formulation is used. The blue dots represent the Greville collocation points.

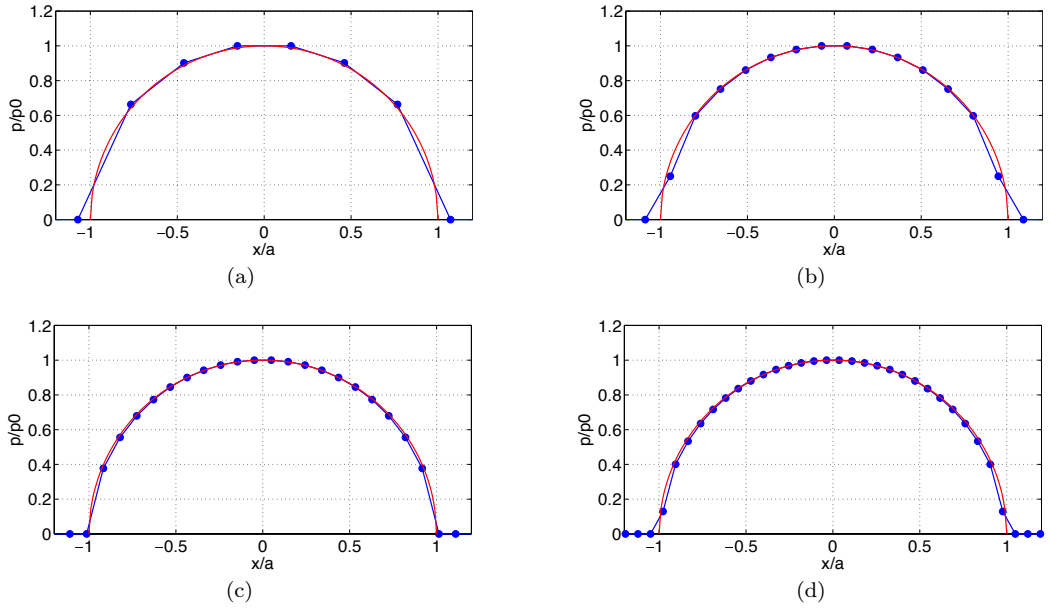

Figure 19: Example C1: analytical and numerical contact pressures for $p_1 = p_2 = 2$, meshes with 50x20 (a), 100x40 (b), 150x60 (c), 200x60 (d) control points. The BC formulation is used.

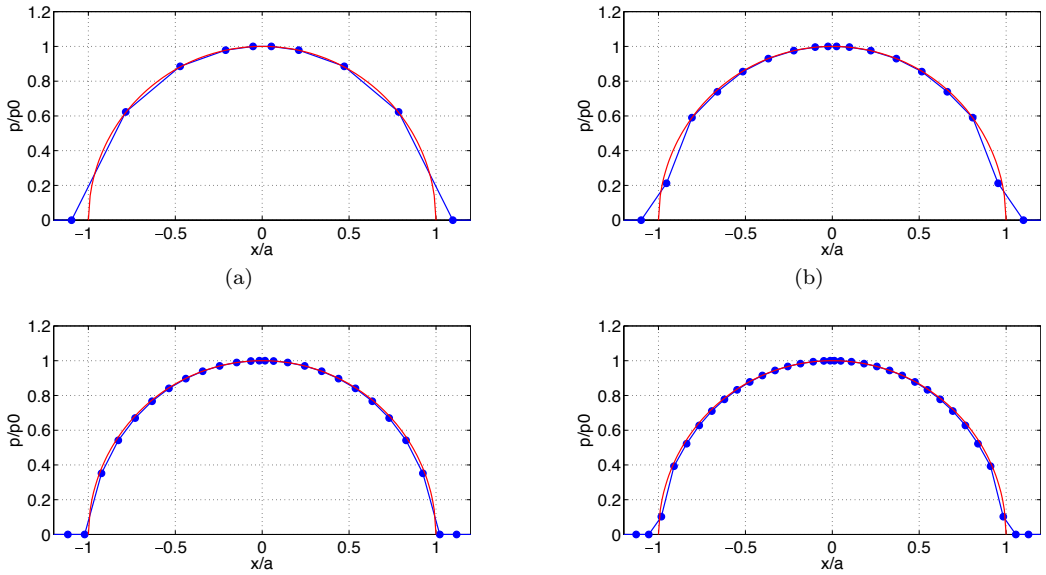

Figure 20: Example C1: analytical and numerical contact pressures for $p_1 = p_2 = 3$, meshes with 50x20 (a), 100x40 (b), 150x60 (c), 200x60 (d) control points. The BC formulation is used.

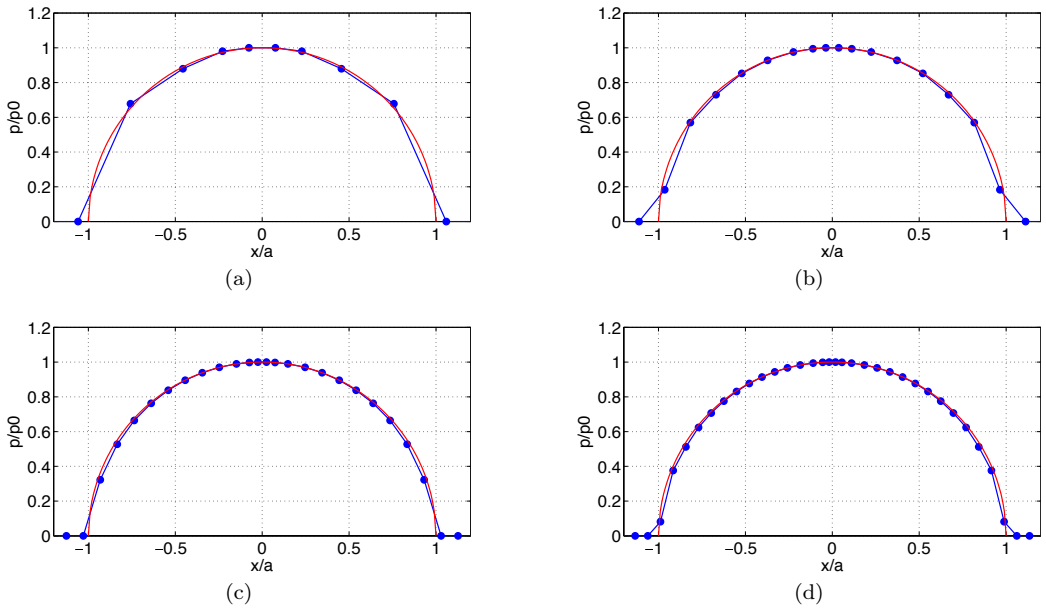

Figure 21: Example C1: analytical and numerical contact pressures for $p_1 = p_2 = 4$, meshes with 50x20 (a), 100x40 (b), 150x60 (c), 200x60 (d) control points. The BC formulation is used.

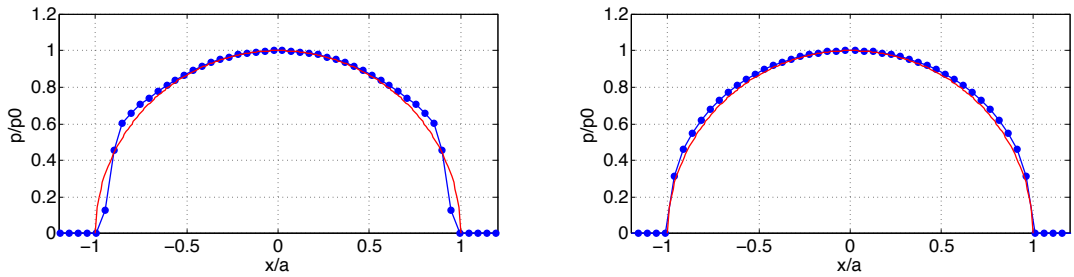

Figure 22: Example C1: analytical and numerical contact pressures for $p_1 = p_2 = 2$, mesh with 150x30 control points, comparison between BC (a) and EC (b) results.

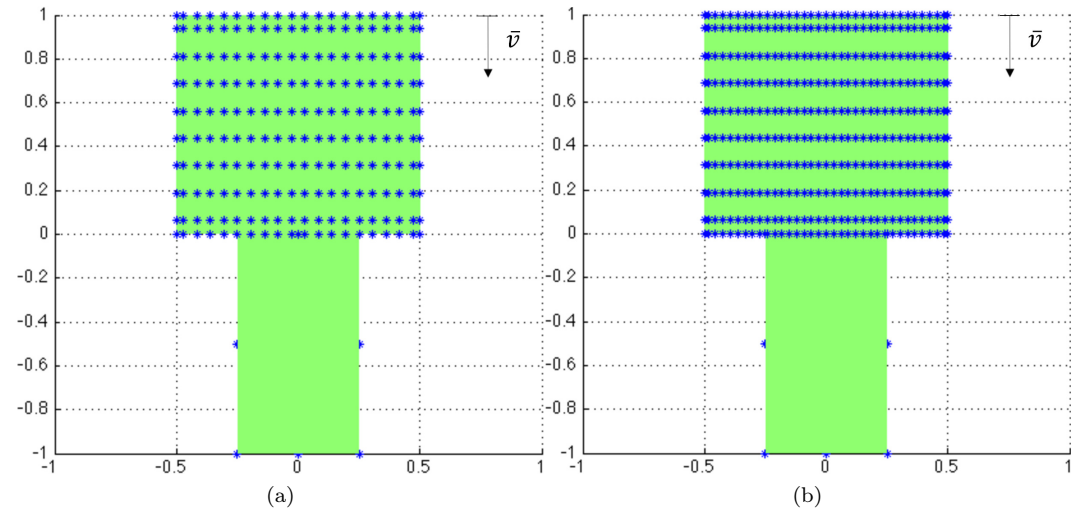

Figure 23: Example C2: the rigid indentor. Mesh 1 with 20x10 control points (a) and mesh 2 with 35x10 control points (b). The blue dots represent the Greville collocation points ($p_1 = p_2 = 2$).

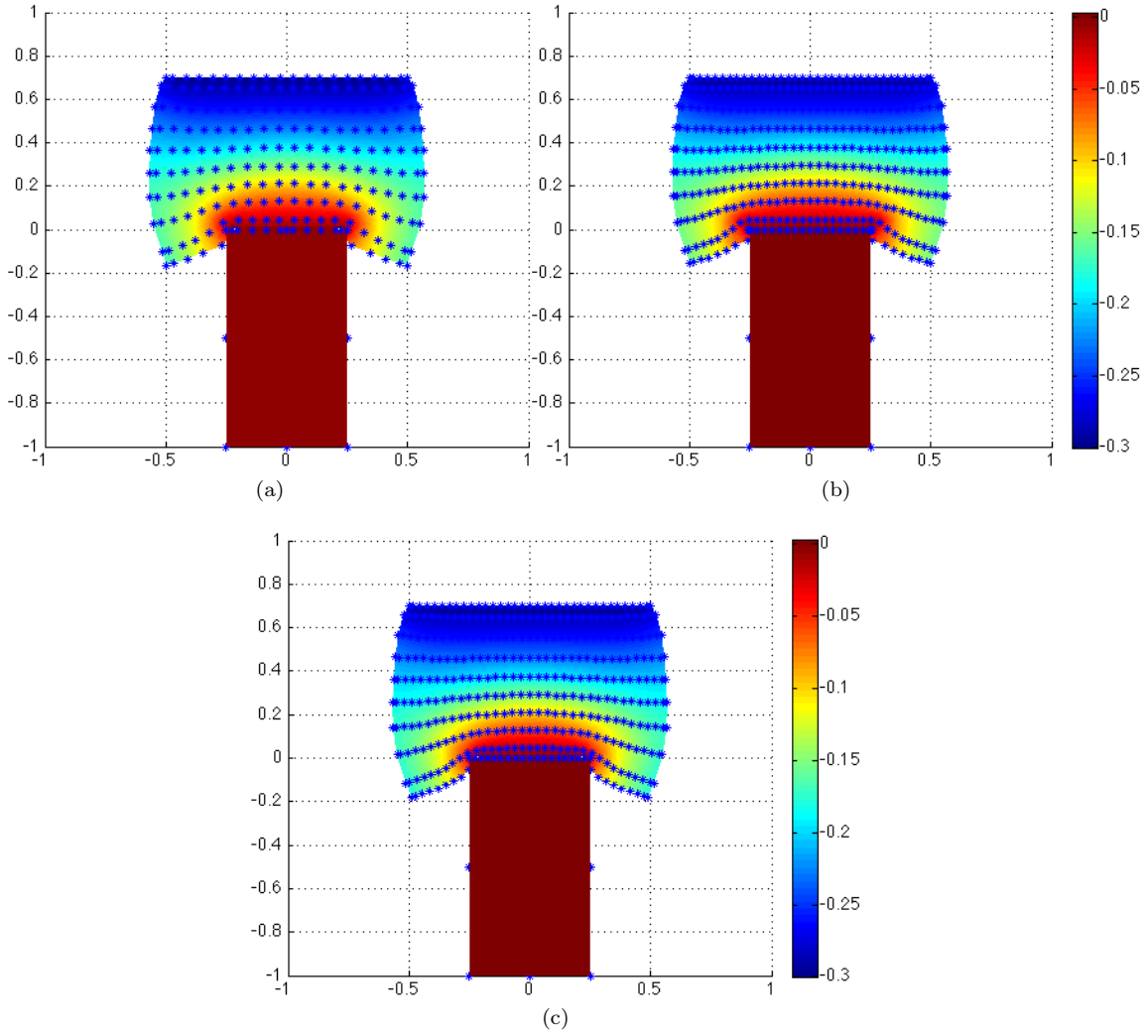

Figure 24: Example C2: vertical displacement contour on the deformed geometry for BC with mesh 1 (a), BC with mesh 2 (b), and EC with mesh 2 (c). The solution in (b) is unconverged. The blue dots represent the Greville collocation points ($p_1 = p_2 = 2$).

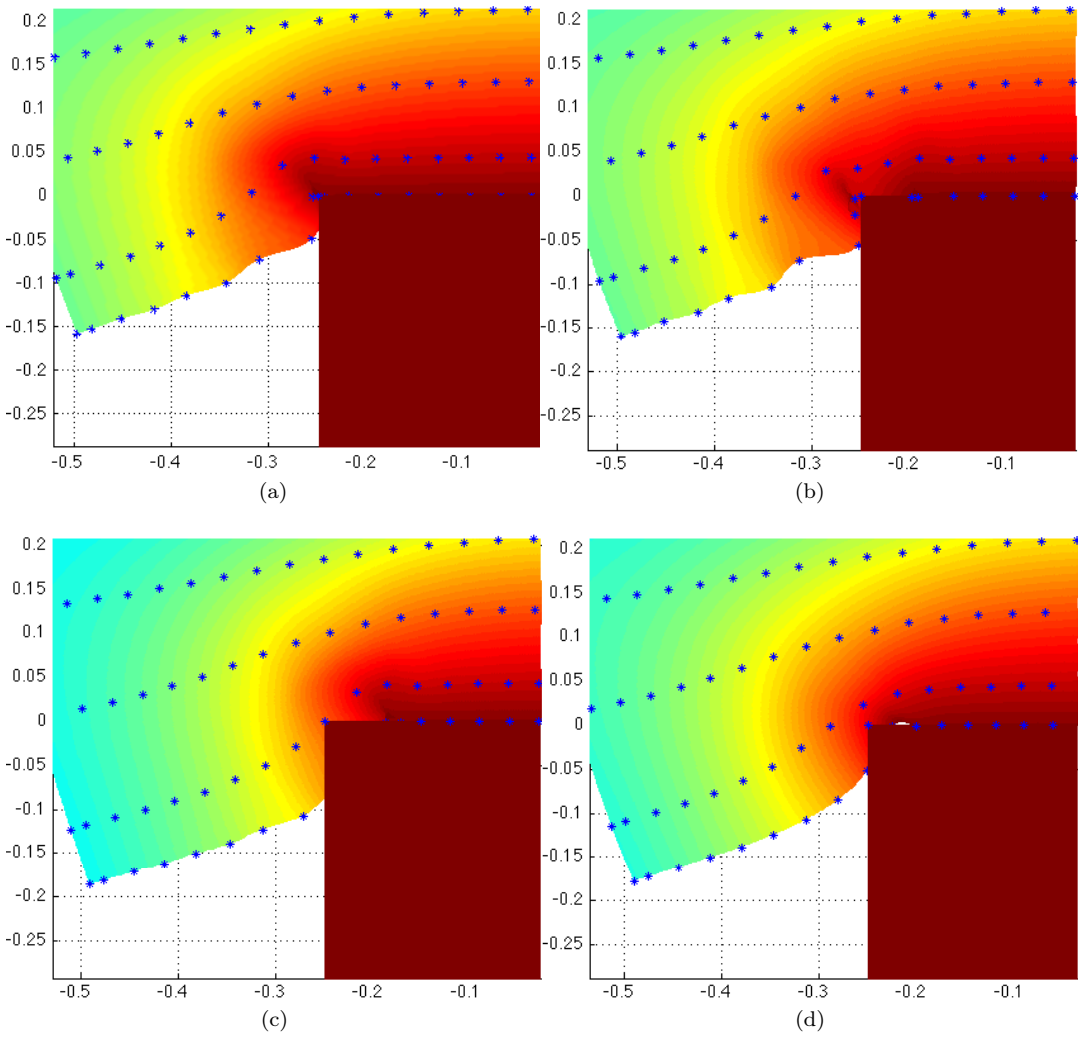

Figure 25: Example C2: close-ups in the vicinity of the corner of the indentor for three subsequent Newton iterations with BC (a,b,c) and at convergence with EC (d). The blue dots represent the Greville collocation points ($p_1 = p_2 = 2$).

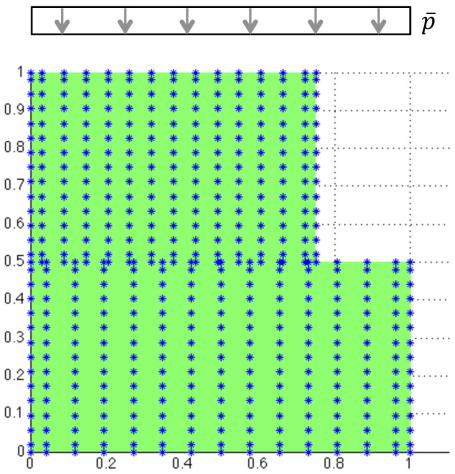

Figure 26: Example C3: the contact patch test. The blue dots represent the Greville collocation points ($p_1 = p_2 = 2$).

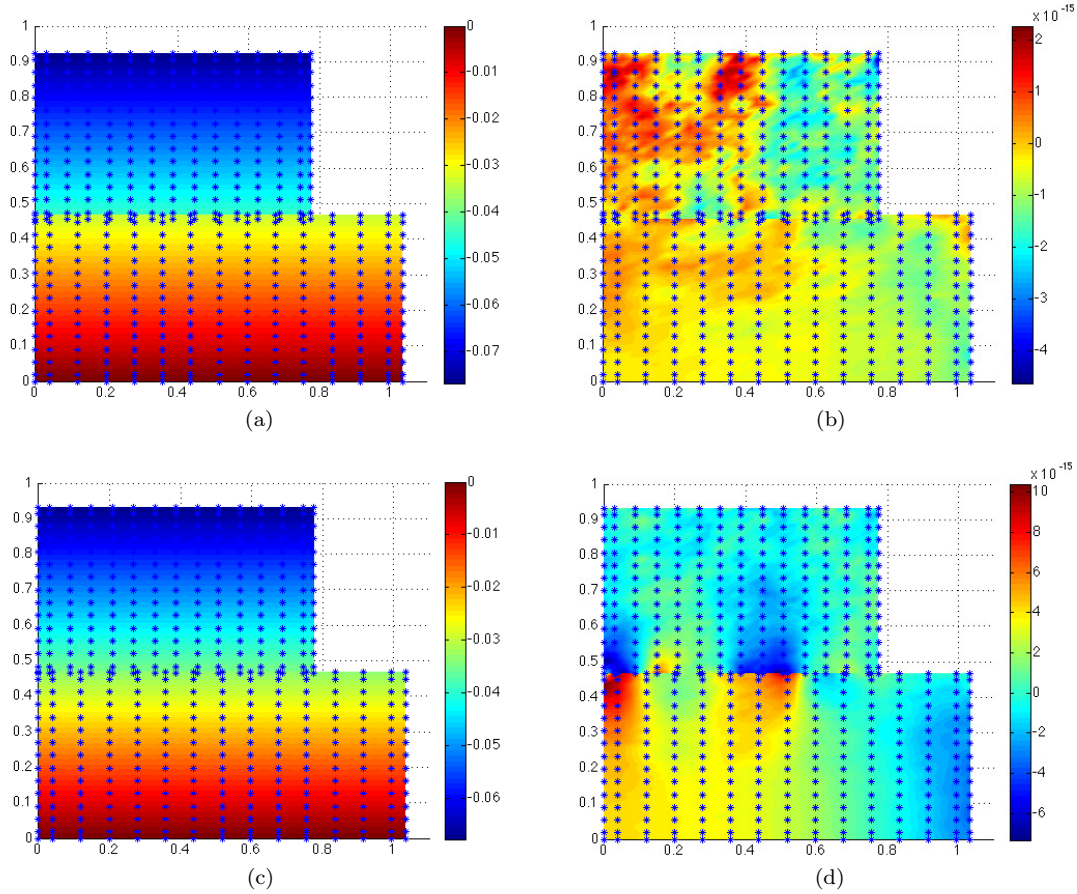

Figure 27: Example C3: vertical displacement contour on the deformed geometry (a,c) and stress error (b,d) for $\varepsilon_N = 10$ (a,b) and $\varepsilon_N = 100$ (c,d). The BC formulation is used. The blue dots represent the Greville collocation points ($p_1 = p_2 = 2$).

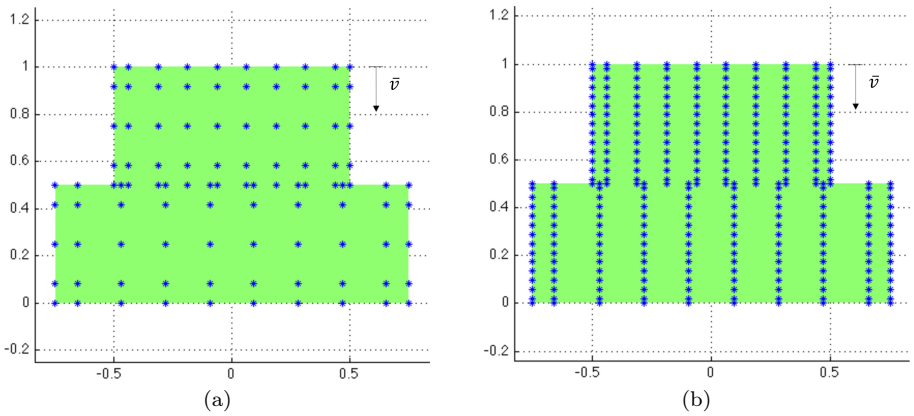

Figure 28: Example C4: the two deformable blocks. Mesh 1 with 10x5 control points (a) and mesh 2 with 10x15 control points (b) for each block. The blue dots represent the Greville collocation points ($p_1 = p_2 = 2$).

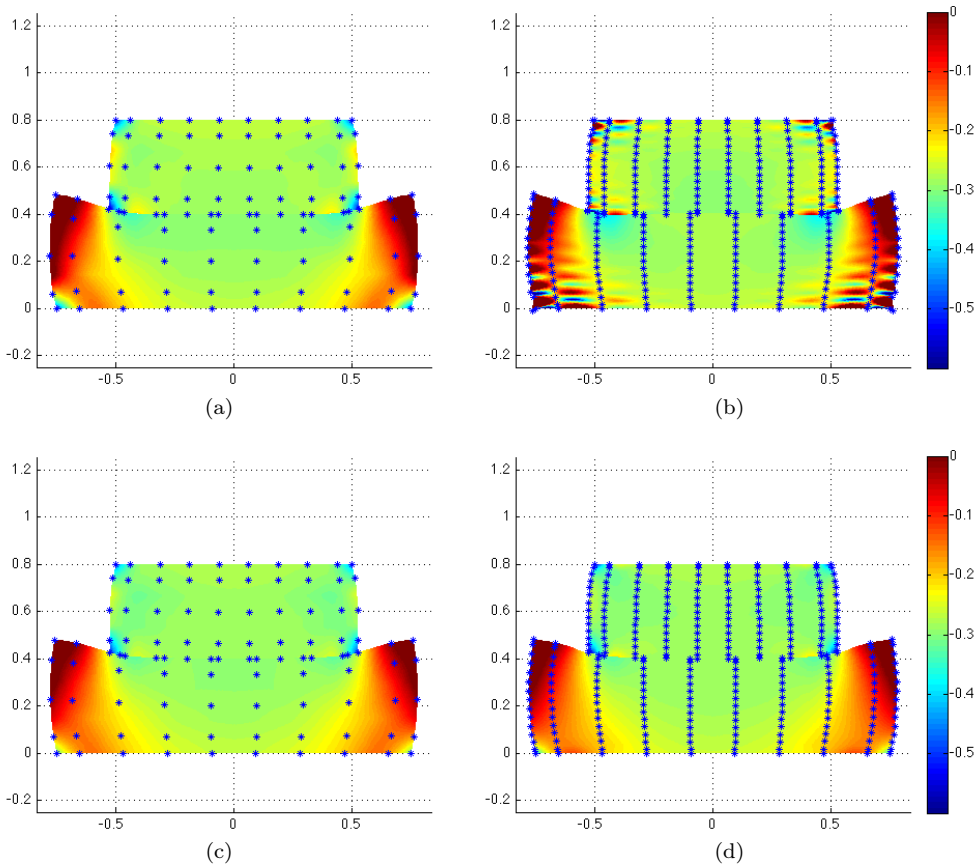

Figure 29: Example C4: contour of stresses σ_y on the deformed geometry for BC with mesh 1 (a), BC with mesh 2 (b), EC with mesh 1 (c) and EC with mesh 2 (d). The blue dots represent the Greville collocation points ($p_1 = p_2 = 2$).

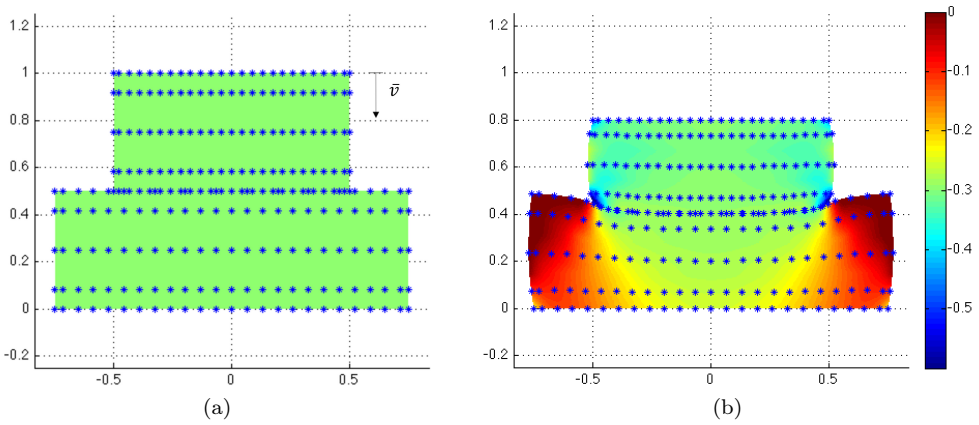

(a) (b)

Figure 30: Example C4: mesh 3 with 25x5 control points for each block (a) and the contour of stresses σ_y on the deformed geometry obtained with EC (b). The blue dots represent the Greville collocation points ($p_1 = p_2 = 2$).